LUNFD6/(NFFL-7218) 2004
January 2004

A trigger for $\mathrm{B_d^0} \to \mathrm{J}/\psi(e^+e^-)\mathrm{K_S}$ in ATLAS and LHCb

Master of Science Thesis
by

Aras Papadelis

LUND UNIVERSITY

DEPARTMENT OF PHYSICS, LUND UNIVERSITY

Abstract

This thesis investigates a trigger for the CP-violating $\mathrm{B}_\mathrm{d}^0 \rightarrow \mathrm{J}/\psi(e^+e^-)\mathrm{K}_\mathrm{s}$ decay in the ATLAS and LHCb experiments at the LHC.

In ATLAS the possibility to use EM clusters (RoIs) to guide the track reconstruction in trigger level 2 is studied (a RoI-guided scan). It is found that this strategy gives lower signal efficiencies than what a track reconstruction in the entire detector (a full-scan) gives. It is also shown that the RoI-guided trigger is able to suppress the trigger rate to feasible levels. The low signal efficiencies are shown to depend on the low efficiency to find both electron RoIs in level 2. An analysis under more realistic conditions is still needed to establish the trigger rates though.

The LHCb study is an inital study of the use of electron clusters from $\mathrm{J}/\psi(e^+e^-)$ in trigger level 1. The probability to find both electrons is investigated and a trigger based solely on cluster information is evaluated. The potential of bremsstrahlung recovery at level 1 is also studied. It is shown that it is possible to suppress the trigger rate to accepted levels. Furthermore, it is possible to correct for bremsstrahlung losses but the efficiency to locate radiated photons is low at level 1.

Contents

1 Introduction and background

Outside Geneva, Switzerland, at the European Laboratory for Particle Physics, CERN, a new accelerator is being built. Upon its completion (at the time of writing scheduled for 2007) it will be able to collide protons at an energy of 7 TeV each, summing up to a centre-of-mass energy of 14 TeV. Since this is the biggest hadron collider built by man so far, it is called the Large Hadron Collider, LHC. Four major experiments are currently being planned and prepared by thousands of physicists from universities all around the world. Two of them, CMS and ATLAS are general-purpose experiments, aiming at exploiting as much as possible of what the accelerator can deliver. This includes searching for the Higgs boson, supersymmetric particles and measuring CP-violation. CP-violation is also the main focus of the third experiment, LHCb, which is dedicated to measuring B-mesons decays with high accuracy, thereby allowing detailed and sensitive measurements of CP-violation in the B system. The fourth experiment, ALICE, is a heavy-ion experiment that will investigate lead ion collisions at LHC.

The purpose of this thesis is to study different aspects of the $\mathrm{B_d^0} \to \mathrm{J}/\psi(e^+e^-)\mathrm{K_s}$ triggers at ATLAS and LHCb. A trigger is a filter that sorts out in real time the vast amounts of uninteresting interactions that occur in a hadron collider and identifies rare interesting events and stores them for later analysis. The first part of the thesis gives an introduction to the theoretical background and concepts used in the thesis. In the second and third part two different trigger analyses are presented, one on ATLAS and one on LHCb. The analyses have in common that they both concentrate on the same decay, namely $\mathrm{B_d^0} \to \mathrm{J}/\psi(e^+e^-)\mathrm{K_s}$.

The ATLAS analysis will evaluate the so called RoI-guided trigger strategy, until now not applied on the $\mathrm{B_d^0} \to \mathrm{J}/\psi(e^+e^-)\mathrm{K_s}$ trigger. The primary goal is to maximise the efficiency of the trigger without consuming too much of the limited computer resources that will be available. In the RoI-guided trigger data from a small fraction of the detector is analysed as opposed to the current plans, the full-scan trigger, where data from the the entire detector volume is used. The primary tools used are electromagnetic calorimetry and tracking.

The LHCb study is an initial study of the possibility to extend the first level trigger of $\mathrm{B_d^0} \to \mathrm{J}/\psi\mathrm{K_s}$ to include the dielectron decay, $\mathrm{J}/\psi \to e^+e^-$ in addition to the dimuon decay. This channel does not have a dedicated trigger yet at level 1. To maximise the calorimeter efficiency, a bremsstrahlung recovery is attempted. Being an initial study, tracking is not included but the analysis is based purely on calorimeter clusters so in some sense the analysis can be seen as an investigation of the potential of a calorimeter based trigger.
To connect the two analyses, one can compare them from a methodological point of view and hopefully learn something about the potential of different triggering techniques.

When working in such big collaborations like ATLAS and LHCb it is easy to focus on one's own work and forget the big picture. The goal with the B-physics programmes at ATLAS and LHCb, to do precise measurements of CP-violation, is one important checkpoint on the road to understanding the baryon asymmetry of

our universe. Without processes like CP-violation matter and antimatter in the early universe would have annihilated each other and there would not be matter left to form galaxies, stars, solar systems and planets. It is the processes behind this asymmetry that has allowed the particles that make up our bodies, our planet and our universe to exist in the way they do today, at least according to the theories that we have. At the end of the day we might be able to understand this, or to formulate it more pompously, we will understand how we ended up here.
And that would not be bad, would it?

1.1 The Standard Model of Particle Physics

The Standard Model of Particle Physics (SM) is a theory about elementary forces and particles that build up our world. It has gradually been formulated within the last 40 years, the main parts during the sixties and seventies. The main concept is that elementary particles in nature are quarks and leptons and that forces are mediated by gauge bosons. Atoms consists of protons and electrons. Protons are not fundamental particles but consist of three quarks, two u-quarks and one d-quark. The electron is called a charged lepton. Other charged leptons are the muon(μ) and tau(τ). Each of the charged leptons have a neutral massless (or very light) neutrino ν associated to them. There also exist other types of quarks. The quark types are often referred to as different *quark flavours*. The leptons and the quarks, can be divided in three families. The three families are defined as:

$$
\begin{array}{lcccc}
 & & & & Charge \\
\text{Quarks :} & \begin{pmatrix} u \\ d \end{pmatrix} & \begin{pmatrix} c \\ s \end{pmatrix} & \begin{pmatrix} t \\ b \end{pmatrix} & \begin{matrix} +2/3 \\ -1/3 \end{matrix} \\
\text{Leptons :} & \begin{pmatrix} \nu_e \\ e \end{pmatrix} & \begin{pmatrix} \nu_\mu \\ \mu \end{pmatrix} & \begin{pmatrix} \nu_\tau \\ \tau \end{pmatrix} & \begin{matrix} 0 \\ -1 \end{matrix}
\end{array} ,
$$

where u, d, ν_e and e belong to the same family. Each of these particles have a twin that is identical to them except for being oppositely charged. These twins are called antiparticles. For instance, the antiparticle of b is $\overline{b}$ (pronounced 'b-bar') and it has a charge of $+1/3$. The antiparticle of the electron is called the positron.
To describe interactions between quarks twelve *gauge bosons* have been introduced. The photon γ is mediating the electromagnetic interactions between charged particles. The weak interaction is mediated by the W^+, W^- and Z^0 bosons. W^+ and W^- can change the flavour of a quark or a lepton, for instance turning an electron into a neutrino via the emission of a W^- boson. The third interaction type in particle physics, the strong interaction, is mediated by eight massless gluons. As their name suggests, they are responsible for 'gluing' the quarks together.

When quarks are 'glued' together they form bound states, *hadrons*. A hadron containing a b or a $\overline{b}$ is called a B-hadron, a term that will be used extensively in this thesis. Generally, when the letter B is combined with another word, like B-trigger or B-physics, it means that a b or a $\overline{b}$ is involved somewhere.
In this thesis three hadrons will be encountered in particular, $\mathrm{B_d^0}$, J/ψ and $\mathrm{K_s}$.

Their quark content is

$$\mathrm{B_d^0} = d\bar{b} \qquad \mathrm{J}/\psi = c\bar{c} \qquad \mathrm{K_s} = s\bar{d} \text{ or } d\bar{s}$$

The reason for $\mathrm{K_s}$ not having a definite quark content is discussed further in Sec. 1.2.1.

Of special interest in a proton-proton collider like LHC is the constituents of the proton. As already mentioned, the proton is made up of two u and one d and by adding the charges of the quarks one find that the charge of the proton is +1. These quarks are called *valence quarks*. Between the quarks, gluons are interchanged constantly. This results in a 'gluon soup' inside the proton. By Heisenbergs uncertainty principle, the gluons can decay into pairs of quarks and antiquarks that exist for short time before they annihilate to form a new gluon. These quark-antiquark pairs are called *sea quarks*. Since they always are created in pairs they do not change to total charge of the proton. The implications of this are very important since they will motivate the need for a trigger when doing experiments with protons.

1.2 CP-violation

CP-violation is one of the fields in particle physics which attracts a lot of attention at the moment. Andrei Sakharov was the first to realize that CP-violation is needed to explain the fact that there are more baryons than antibaryons in the universe. In Sec. 1.2.1 the concepts of C, P and CP-violation are explained in a historical context. Sec. 1.2.2 contains a more technical description of how CP violation is described within the framework of the Standard Model. Some knowledge of the formalism of the Standard Model is needed to understand that section.

1.2.1 Experiments in the past

The laws of physics are to great extent based on symmetries and invariance of a physical system under certain transformations. For example, rotational invariance leads to the conservation of angular momentum.
A parity transformation on a system means turning a right handed coordinate system to a left handed one, i.e. reflecting the position of every particle in the origin:

$$x_i \rightarrow x_i^{'} = -x_i$$

While parity is conserved in strong and electromagnetic interactions, Wu and coworkers in 1957, after a proposal from Lee and Yang, showed that parity is violated in the β-decay of Cobolt-60 nuclei[1]. From this it could be concluded that parity is violated in weak interactions, the interaction type that is associated with β-decays.
Parity(P) is not the only symmetry that is broken in weak interaction. Goldhaber and coworkers in 1958 measured the helicity[1] of the neutrino and found that only left-handed neutrinos interact via weak interaction[2]. Later it was also shown that

[1] The helicity of a particle is defined by the direction of its spin component along the direction of motion. If the spin component is pointing in the same direction as the momentum vector, the particle has a *right-handed* helicity. The opposite is called *left-handed* helicity.

only right-handed antineutrinos participate in weak interactions[3]. The conclusion is that all systems are not invariant under charge conjugation (C-invariance). The operation of charge conjugation(C) means replacing all particles in a system with their antiparticles, not changing anything else (like spin and momentum). If C-invariance were true for weak interactions then neutrinos and antineutrinos would behave in an identical way, which is not the case.
An example of the decays where C and P are violated is

$$\mu^- \rightarrow e^- + \overline{\nu}_e + \nu_\mu$$

and

$$\mu^+ \rightarrow e^+ + \overline{\nu}_\mu + \nu_e$$

Although both C and P were found to be violated separately, the combined operation of CP on a system seemed to be a conserved symmetry. CP symmetry means that a left-handed neutrino interacts in the same way as a right-handed anti-neutrino. Experiments on the neutral kaon system in 1964 however showed that also CP-invariance is violated, although to a very small extent[4]. What makes the neutral kaon system so special is that can oscillate between K^0 and $\overline{\mathrm{K}^0}$ via weak interaction. The particles that are observered in a laboratory are not K^0 and $\overline{\mathrm{K}^0}$ but $\mathrm{K_s}$ and $\mathrm{K_L}$, two particles with nearly equal masses but with different decay modes and lifetimes. They are thought of as being linear combinations of K^0 and $\overline{\mathrm{K}^0}$.
While $\mathrm{K_s}$ primarily decays into two-pion states with a CP-eigenvalue=1, $\mathrm{K_L}$ primarily decays into final states with CP=-1. Assuming that CP is always conserved, this suggests that $\mathrm{K_s}$ and $\mathrm{K_L}$ are the CP-eigenstates of the K^0-$\overline{\mathrm{K}^0}$ system. What was discovered in 1964 though, was that $\mathrm{K_L}$ also, rarely (B=0.003), decays into a two-pion final state (CP=1) meaning that CP is not conserved in all interactions.

1.2.2 CP-violation in the Standard Model

In this section some of the theory for CP-violation(CPV) in the Standard Model(SM) is reviewed.
In the SM, particles acquire their mass via interaction with a neutral scalar Higgs field. This is called the Higgs Mechanism. The mass eigenstates that participate in this interaction are not the same as the eigenstates participating in electroweak decays, the electroweak eigenstates. This was understood from experiments. When a particle is observed in a laboratory it is the mass eigenstate that is observed. For instance, the weak kaon decay

$$K^-(s\overline{u}) \rightarrow \mu^- + \overline{\nu}_\mu$$

can be described by a Feynman diagram with a $\overline{u}sW$-vertex. This kind of vertex, where quarks from different families are involved, are not present in the part of the SM Lagrangian that describes electroweak interactions. The eigenstates in the electroweak Lagrangian can thus *not* be the same eigenstates as the observed mass eigenstates. If they were to be identical no quark interactions between families would be allowed in the weak decay. Instead the assumption is made that the electroweak eigenstates are linear combinations of the mass eigenstates. So, in the kaon decay it is not the s-quark that participates but s', a linear combination of the d, s and b quarks. The charged current in the Standard Model Lagrangian changes:

$$J^{\mu}_{ch} = \begin{pmatrix} \overline{u} & \overline{c} & \overline{t} \end{pmatrix} \gamma^{\mu} P_L \begin{pmatrix} d \\ s \\ b \end{pmatrix} \longrightarrow \begin{pmatrix} \overline{u} & \overline{c} & \overline{t} \end{pmatrix} \gamma^{\mu} P_L \begin{pmatrix} d' \\ s' \\ b' \end{pmatrix}$$

where

$$\begin{pmatrix} d' \\ s' \\ b' \end{pmatrix} = \begin{pmatrix} V_{ud} & V_{us} & V_{ub} \\ V_{cd} & V_{cs} & V_{cb} \\ V_{td} & V_{ts} & V_{tb} \end{pmatrix} \begin{pmatrix} d \\ s \\ b \end{pmatrix} = \mathrm{V_{CKM}} \begin{pmatrix} d \\ s \\ b \end{pmatrix}$$

and $\gamma^{\mu} P_L$ describe the interaction.
The coefficient matrix is called the Cabibbo-Kobayashi-Maskawa(CKM) matrix after the men that introduced it. Cabibbo introduced it for two quark families and Kobayashi and Maskawa extended it to three families. Vertices of type dtW or cdW now appear in the charge current. For instance, the dtW vertex corresponds to a charged current of type

$$\bar{t}\gamma^{\mu} P_L V_{td} d$$

As can be seen from $\mathrm{V_{CKM}}$, only the down-type quarks are redefined. The up-type quarks u,c and t are by convention fixed so that the mass and electroweak eigenstates are equal. The size of the coefficients in $\mathrm{V_{CKM}}$ determine the probability for a certain up-type quark to participate in a reaction with a certain down-type quark. In the kaon decay, V_{us} is involved. The elements of $\mathrm{V_{CKM}}$ can only be determined experimentally.

Being a 3×3 matrix, $\mathrm{V_{CKM}}$ can have 9 free parameters. From group properties of $\mathrm{V_{CKM}}$ the number of free parameters can be reduced to four, three real angles and one complex phase. $\mathrm{V_{CKM}}$ can be expressed in the Wolfenstein parameterization as a polynomial function of $\sin\theta_c$ where θ_c is the Cabibbo angle[2]. Experimentally, $\lambda = \sin\theta_c$ has been measured to be approximately 0.22 . The parameterization is:

$$\mathrm{V_{CKM}} = \begin{pmatrix} 1-\lambda^2/2 & \lambda & A\lambda^3(\rho - i\eta) \\ -\lambda & 1-\lambda^2/2 & A\lambda^2 \\ A\lambda^3(1-\rho-i\eta) & -A\lambda^2 & 1 \end{pmatrix} + \mathcal{O}(\lambda^4)$$

In this parameterization many interesting things can be seen. First of all, one can notice that the diagonal terms, i.e. the ones that participate in decays within the same quark family, are all of the order of 1, furthermore they do not contain any complex factors. It is the parameter η that is the complex phase.
What is the connection between $\mathrm{V_{CKM}}$ and CPV? In any good quantum field theory the combined operation of CPT (where T means time reversal) must leave a system invariant. So, if CP is is violated in a process, also T has to be violated in the process. Since time reversal, i.e. letting $t \to -t$ can be seen as complex conjugation of a system, only complex terms in the Lagrangian allow CPV. In the SM, this complex

[2]The Cabibbo angle is the only free parameter if the quark mixing matrix V is written down for the first two quark generations, i.e. if V is a 2×2 matrix.

quantity is identified as the phase η in $\mathrm{V_{CKM}}$. Following this, for an interaction to be CP-violating it has to be related to complex CKM terms. The position of the complex quantity in $\mathrm{V_{CKM}}$ depends on the parameterization but following the Wolfenstein parameterization one should look for CP-violating decays where V_{td} and V_{ub} are included (at least to $\mathcal{O}(\lambda^3)$, if higher orders of λ are included then η appears in other vertices too).

1.2.3 CP-violation in the neutral B-system and the Unitarity Triangle

Now that the origin of CPV in the SM has been identified the next question should be: how can this be used to measure CPV? As $\mathrm{V_{CKM}}$ was introduced, it should be a unitary matrix, i.e.

$$\mathrm{V_{CKM}}\mathrm{V_{CKM}^{\dagger}} = \begin{pmatrix} V_{ud} & V_{us} & V_{ub} \\ V_{cd} & V_{cs} & V_{cb} \\ V_{td} & V_{ts} & V_{tb} \end{pmatrix} \begin{pmatrix} V_{ud}^* & V_{cd}^* & V_{td}^* \\ V_{us}^* & V_{cs}^* & V_{ts}^* \\ V_{ub}^* & V_{cb}^* & V_{tb}^* \end{pmatrix} = \begin{pmatrix} 1 & 0 & 0 \\ 0 & 1 & 0 \\ 0 & 0 & 1 \end{pmatrix}$$

This condition leads to a set of equations of which six are orthogonality relations. Depending on which matrix elements in $\mathrm{V_{CKM}}$ that are included the orthogonality relations can be linked to certain decays. To describe properties of the neutral B-system the relation

$$V_{ud}V_{ub}^* + V_{cd}V_{cb}^* + V_{td}V_{tb}^* = 0 \tag{1}$$

can be used. This relation is special compared to the others because the three terms are of the same order of λ. Each of the terms in the relation has a real and a complex part and can thus be viewed as a vector in the complex plane. Since the sum of these three vectors should add up to 0 this can be depicted as a triangle drawn in the complex plane. If only terms to $\mathcal{O}(\lambda^3)$ are kept and the vectors are normalised to $A\lambda^3$ this gives the triangle in Fig. 1. The three angles in this triangle are in the literature referred to as α,β and γ. The amount of CP-violation in the SM lies in the size of η. If α,β and γ can be measured this would give the size of ρ and η. Therefore the current investigations around CPV are concentrating on the angles in the unitarity triangle rather than the angles and phase of $\mathrm{V_{CKM}}$. Another reason for paying interest to measuring the three angles is that if α, β and γ do not sum up to 180° this is a signal of some underlying new physics.
The orthogonality relation connected to the neutral K-system has terms of different orders of λ giving a very 'squashed' triangle where the angles are impossible or at least very hard to measure.

To measure the angles of the unitarity triangle, one has to determine the length of the sides. Of special interest in this thesis is the length of the side AB, conventionally denoted R_t. Using that $V_{ud} \approx V_{tb}^* \approx 1$ and $V_{cd} \approx -\lambda$ Eq. 1 becomes

$$V_{ub}^* - \lambda V_{cb}^* + V_{td} \approx 0 \Rightarrow \frac{V_{ub}^*}{\lambda V_{cb}^*} - 1 + \frac{V_{td}}{\lambda V_{cb}^*} \approx 0 \quad .$$

These three terms are the vectors in the triangle, the third being the vector from A to B. Following this, the length R_t is

$$R_t = \frac{1}{\lambda}\left|\frac{V_{td}}{V_{cb}}\right| \quad .$$

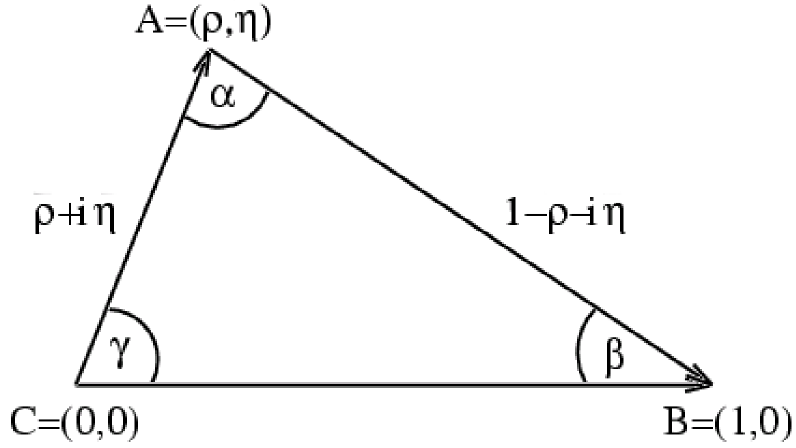

Figure 1: *The unitarity triangle corresponding to Eq. 1, normalised to* $A\lambda^3$

To measure the angle β the elements V_{td} and V_{cb} are needed. These two coefficients can be found in the decay $\mathrm{B_d^0} \rightarrow \mathrm{J}/\psi\mathrm{K_s}$. In Fig. 2a the direct decay of $\overline{\mathrm{B_d^0}}$ is shown. Fig. 2b shows the process of $\mathrm{B_d^0}$-$\overline{\mathrm{B_d^0}}$ oscillation that introduces V_{td} vertices in the decay. Whether the decay occurs as a $\mathrm{B_d^0}$ or a $\overline{\mathrm{B_d^0}}$ the same final state can be reached. The quantum mechanical interference between the direct and the 'oscillated' decay will lead to CPV. The amount of CPV can be measured with the observable A which can be shown to be proportional to $\sin 2\beta$, where β is the angle in the unitarity triangle in Fig 1 and A is defined to be:

$$A = \frac{\Gamma(\mathrm{B_d^0} \rightarrow \mathrm{J}/\psi\mathrm{K_s}) - \Gamma(\overline{\mathrm{B_d^0}} \rightarrow \mathrm{J}/\psi\mathrm{K_s})}{\Gamma(\mathrm{B_d^0} \rightarrow \mathrm{J}/\psi\mathrm{K_s}) + \Gamma(\overline{\mathrm{B_d^0}} \rightarrow \mathrm{J}/\psi\mathrm{K_s})}$$

The current world average (August 2003)[5] is

$$\sin 2\beta = 0.701 \pm 0.053$$

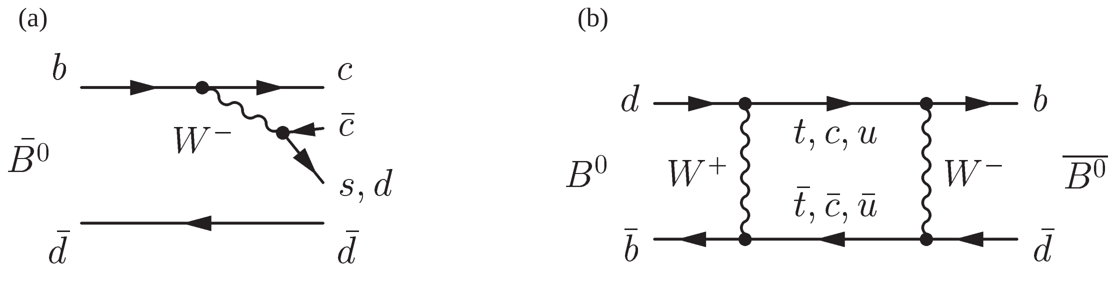

Figure 2:
a) The direct decay of $\overline{\mathrm{B_d^0}} \rightarrow \mathrm{J}/\psi(c\bar{c})\mathrm{K_s}(s\bar{d})$.
b) The diagram for $\mathrm{B_d^0}$-$\overline{\mathrm{B_d^0}}$ *mixing.* $\mathrm{B_d^0}$ *and* $\overline{\mathrm{B_d^0}}$ *can decay into the same final state.*

1.3 Concepts and tools in experimental high energy physics

This section contains a brief review of some of the important concepts and definitions that will be used in the thesis.

1.3.1 Position and momentum measurements

The position of a particle in a detector at a given instance is defined by three coordinates. If the interaction point is taken to be the origin of the coordinate system the convention is to define the z-axis to run along the direction of the beam pipe. The other two coordinates are chosen according to the design of the detector. In ATLAS, being a barrel detector covering the entire 4π-space, a polar coordinate system is often used, with azimuthal angle ϕ, measured around the beam axis and polar angle θ from the beam axis. Although this seems to be the most natural choice of coordinates, it is not what is conventionally used at hadron colliders. The azimuthal angle θ is substituted with the the *pseudorapidity* because the particle multiplicity in the detector is roughly constant in units of pseudorapidity. The pseudorapidity can be derived from the *rapidity* of a particle:
When dealing with relativistic particles, the velocity v of a particle is not invariant under Lorentz-transformations. Instead, the rapidity, defined as

$$y \equiv \tanh^{-1} v$$

turns out to be a useful quantity since is frame independent. The y in this definition should not be confused with the Cartesian coordinate y. For a particle with a certain energy E and a momentum component $p_{\rm L}$along the beam pipe the rapidity can be rewritten as

$$y = \frac{1}{2} \ln \frac{E + p_{\rm L}}{E - p_{\rm L}} \quad .$$

At relativistic energies, the concept of pseudorapidity is often used instead. It is defined to be

$$\eta \equiv -\ln \tan(\theta/2) \tag{2}$$

and it to good approximation equal to y at the energies that LHC will run at. As can be seen, η is a quantity that depends on θ. η is conventionally used used instead of θ to parametrize the detector. Table 1 shows an example of the non-linear relation between θ and η.

$\theta[°]$	90	45	40.4	15.4	15	10	5.7	2.1	0
η	0	0.88	1	2	2.03	2.44	3	4	∞

Table 1: *A conversion table between the azimuthal angle θ and the pseudorapidity η. θ runs between $[0, 180]$ when η runs between $(-\infty, +\infty)$.*

A distance in the $\eta\phi$-space is defined to be

$$\Delta R = \sqrt{(\Delta\eta)^2 + (\Delta\phi)^2} \quad . \tag{3}$$

Also, using that

$$\sin\theta = 1/\cosh\eta$$

the momentum component in the plane transverse to the beam axis can be written as

$$p_{\mathrm{T}} = \frac{|\mathbf{p}|}{\cosh \eta}$$

This quantity, the transverse momentum, is used extensively in experimental high energy physics. Although the energy E is not a vector the transverse energy can be defined analogously to be

$$E_{\mathrm{T}} = \frac{E}{\cosh \eta}$$

1.3.2 The invariant mass

A very useful concept in high energy physics is that of the *invariant mass*. Consider a system of N particles where every particle has energy E_i and momentum $\mathbf{p}_i$. The Lorenz invariant expression

$$W^2 = \left(\sum_i^N (E_i)\right)^2 - \left(\sum_i^N (\mathbf{p}_i)\right)^2$$

can the be formed. W is called the invariant mass of the system. A system that initially contains one particle X will have

$$W^2 = E_X^2 - \mathbf{p}_X^2 = m_X^2.$$

Now, let X decay into a final state of two particles. Since W is frame-invariant and energy and momentum must be conserved in the decay, one obtains:

$$m_X^2 = W^2 = (E_1 + E_2)^2 - (\mathbf{p}_1 + \mathbf{p}_2)^2. \tag{4}$$

So, by knowing the energy and momentum of each of the final state particles it is possible to calculate in mass of the particle in the initial state. This is very powerful technique when looking for short-lived particles that decay before they can be detected.

1.3.3 Interaction rates and available energy

The probability for a physical process to occur can be expressed in terms of the cross-section of that particular process. The rate dN/dt that a process occurs with depends on its cross-section σ and the instantaneous luminosity $\mathcal{L}$ of the accelerator:

$$\frac{\mathrm{dN}}{\mathrm{dt}} = \sigma \mathcal{L} \tag{5}$$

The cross-section is among other thing depending on the energy that is available to produce particles. Since LHC is a symmetric collider both protons will have oppositely directed three momenta $\mathbf{p}$. The total centre-of-mass energy $\sqrt{s}$ is thus

$$\begin{aligned} s &= (p_1 + p_2)^2 \approx 2p_1 \cdot p_2 = 2(E^2 - \mathbf{p} \cdot (-\mathbf{p})) \approx 4E^2 \implies \\ \sqrt{s} &= 2E \end{aligned}$$

where $p_{1,2} = (E, \pm\mathbf{p})$ are the four momenta of the incoming protons.
At LHC each proton will be accelerated to an energy of 7 TeV meaning that $\sqrt{s}$=14 TeV. When the protons 'collide' this energy can be used to create new particles. In practice, since the protons are not elementary particles but contain quarks, gluons and sea quarks, all of the CM-energy will not be available to produce new particles, some parts of the proton will not participate in the interaction and continue along the beam line.

1.4 B-physics at LHC

Running at a centre-of-mass energy of $\sqrt{s} = 14$ TeV the production cross-section of $b\bar{b}$ pairs is expected to be of the order of 500 μb [6]. It is estimated that about one collision in every hundred will produce a b-quark pair. With a start-up luminosity of $2 \cdot 10^{33}$ cm^{-2}s^{-1} LHC can indeed be called a B-factory, capable of doing competitive B-physics. The existing B-factories, BaBar(SLAC) and BELLE(KEK), are e^+e^- colliders operating in the $\Upsilon(4S)$ region. By doing this they cannot access the B_s system necessary to study all the angles of the unitarity triangle (Fig. 1). The very broad spectrum of B-decays available at LHC will make it possible to make many independent measurements of the same angle. The possibility to do this makes it easier to minimise the systematic errors in the measurements and to also to find indications of new physics.

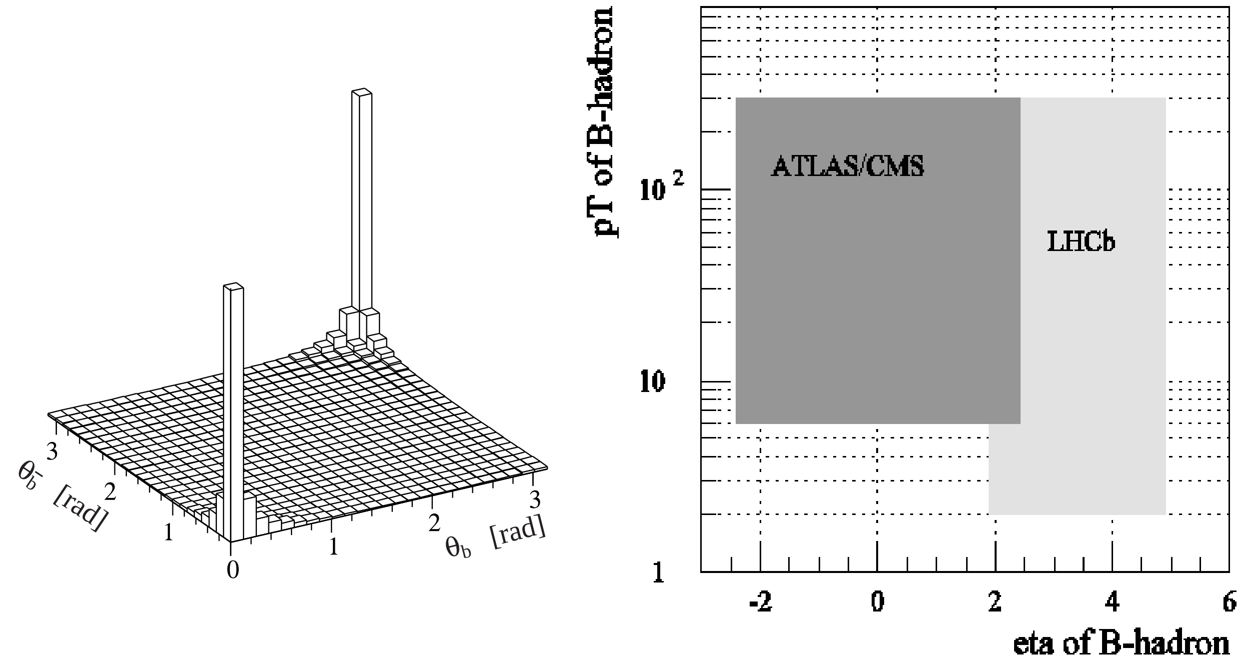

(a) (b)

Figure 3:
a) Polar emission angles of B-hadrons and $\overline{\mathrm{B}}$-hadrons. [7]
b) LHCb and ATLAS complement each other in η and p_T coverage

Although LHCb is a dedicated experiment for B-physics, both ATLAS and CMS also have a B-programme. Simulations of the $b\bar{b}$-production at LHC have shown that B-hadrons predominantly are produced in a in a cone around the beam direction. In Fig. 3a the polar angle θ at which B-hadrons and $\overline{\mathrm{B}}$-hadrons[3] are emitted is shown[7]. The LHCb detector is not designed with a 4π-coverage as ATLAS but rather as a one-arm spectrometer covering a pseudorapidity range of of $1.9 \leq \eta \leq 4.9$ (10 mrad $\leq \theta \leq$ 300 mrad) in respect to the beam pipe. This should be compared to the ATLAS η-coverage of $|\eta| \leq 2.4$ [4]. As can be seen in Fig. 3b, ATLAS and LHCb complement each other well in η and p_{T} coverage.

1.5 The need for a trigger

In e^+e^- colliders like LEP(CERN) the accelerated electrons and positrons each carry half of the CM-energy each. But, as a consequence of colliding protons, the CM-energy will be shared between all the proton constituents and most of the constituents will be 'soft', i.e. they only carry a small fraction of the total energy of the proton. As a result of this is the majority of the interactions taking place will not be 'hard', like in a lepton collider, but soft. It is the hard interactions that are interesting when one is studying B-physics or looking for new particles. Of the hard interactions, which are just a small fraction of the total number of interactions, only a few will be interesting. Therefore, some kind of filter is needed to find the interesting interactions. This filter is the trigger. Each experiment at LHC will have its own trigger, tailored to suit the particular needs of the experiment. For every type of interesting reaction a trigger analysis has to be done to find the 'fingerprint' of that reaction. The decay $\mathrm{B}_{\mathrm{d}}^0 \rightarrow \mathrm{J}/\psi(e^+e^-)\mathrm{K}_{\mathrm{s}}$ is the particular reaction that is studied in this thesis.

2 Analysis on ATLAS

2.1 The ATLAS experiment

The ATLAS experiment is the biggest collaboration so far in the history of physics and basic research. Over 2000 physicists from universities and laboratories in 34 countries worldwide are participating in the project. Being a general-purpose detector of big size, it contains a large variety of different subdetectors and two separate magnetic systems. Fig.4 gives an overview of the detector.

The dimensions of the detector are defined by the muon system. The outermost layers of the forward muon chambers are located about 23 m from the interaction point and the outer chambers of the barrel are at a radius of about 11 m. The muon chambers are embedded between the barrel toroid magnets which are able to deliver a magnetic field of 4.1 T. The muon trigger chambers cover a pseudorapidity range of $|\eta| \leq 2.4$. Between the toroid magnets and the central solenoid, the calorimeter system is located. The barrel calorimeters combined with the end-cap calorimeters can cover a pseudorapidity range up to $|\eta|$=4.9. The central solenoid provides the

[3]With $\overline{\mathrm{B}}$-hadron a hadron with a b-quark is meant.

[4]The total η-coverage of ATLAS is bigger but for the B-physics only $|\eta| \leq 2.4$ will be used, see Sec. 2.1 for more details.

Inner Detector (ID) with a solenoidal field of 2T. The ID is contained within a cylinder of length 7 m and a radius of 1.15 m. With its three separate tracking detectors, its purpose is to provide high-precision measurements of position and momentum. The semi-conductor pixel detector is located closest to the interaction point. With its high granularity it is capable find displaced vertices from B-hadron and τ decays. The semiconductor tracker (SCT) follows the pixel detector. Together with the transition radiation tracker (TRT) its task is form tracks of charged particles traversing the ID. As the name implies, the TRT also measures transition radiation which can be used to separate electrons from pions. The η-coverage of the ID is $|\eta| \leq 2.5$ which sets the limit for physics reconstruction with tracks, including the B-programme.

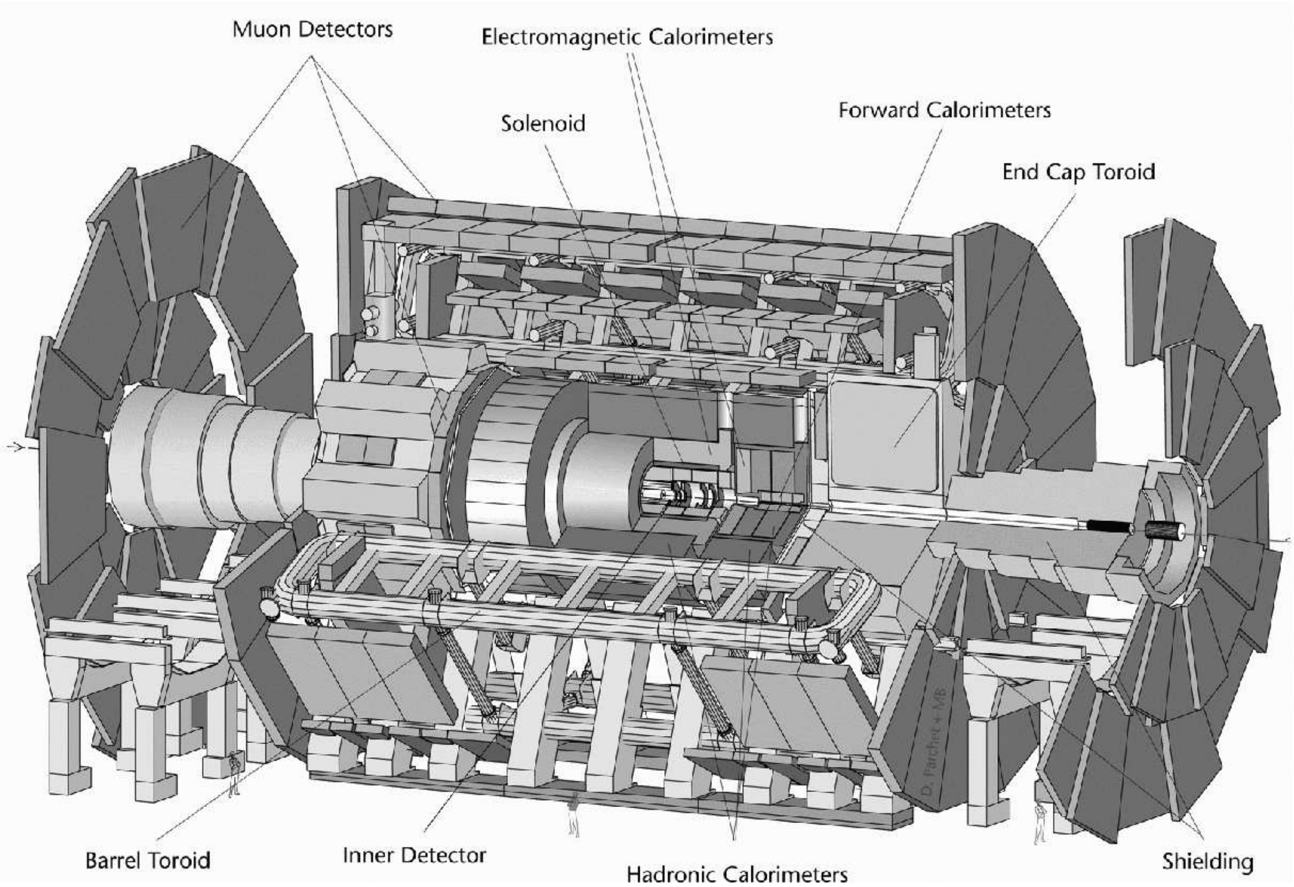

Figure 4: *The ATLAS detector with its subdetectors.*

2.2 The ATLAS trigger

With a bunch-crossing rate of 40 MHz an interaction rate of 10^9 Hz is expected when the design luminosity of 10^{34} cm^{-2}s^{-1} is reached[5], corresponding to total inelastic, non-diffractive proton-proton cross-section of 70 mb [8]. The average event size is expected to be around 1 MByte [9] meaning that if every event was to be stored for later analysis, it would result in 1 PByte of data output per second. With the technology of today (and of many years to come), it is impossible to handle a dataflow of that magnitude. Instead, the event storage rate is limited to approximately 100 Hz, meaning that a rate reduction of seven orders of magnitude has to be achieved. There is an obvious need for a trigger system. The challenge of this trigger is to select as many interesting events as possible, while sorting out the uninteresting ones. What is meant an 'interesting' event is governed by what the experiment aims to observe. In the case of ATLAS, it is of high priority to find one or more Higgs bosons, thereby increasing the understanding of the origin of electroweak symmetry breaking. It is also important that ATLAS can detect and measure signs of new physics (like supersymmetric particles), this includes the ability to detect reactions that currently have not been modelled.

The ATLAS trigger is divided into three levels, level-1 (LVL1), level-2 (LVL2) and the Event Filter (EF). LVL2 and EF are often referred to as the High-Level Trigger (HLT). The main difference between the trigger levels is the amount of time each level has at its disposal to perform the required analysis of the event and then decide whether to keep the event or discard it. This time is called the latency of the trigger. The distance from the interaction point to the muon stations gives a time-of-flight of the muons comparable to the bunch-crossing period.Furthermore, a pulse in the calorimeter extends over many periods. This, in combination with the time it takes for the electronics and hardware-implemented trigger algorithms to form the trigger decision, results in a LVL1 latency of 2.0 μs (to be compared with the bunch crossing period of 25 ns). This time also includes the time that is required to send the signals between the different steps in the trigger. To minimise this time the LVL1 electronics are located very close to the detector. Running at high luminosity results in a high rate of interactions leading to high track multiplicities at each bunch crossing. The B-trigger is not designed to handle such high multiplicities and for this reason, the main part of the B-physics programme is planned to take place during the first years of operation when the luminosity is low, i.e. $2 \cdot 10^{33}$ cm^{-2}s^{-1}. As a result of this, the mean interaction rate will be lower than for the design luminosity, about five inelastic interactions per collision, giving at total interaction rate of 10^8 Hz. So, for every interesting event there will be on the average four uninteresting events superimposing the interesting one. These uninteresting events are called *pile-up events*. When designing the trigger this has to be taken into account. Rates and latencies of the three trigger levels are shown in Fig. 5.

At low luminosity, the task of the LVL1 trigger is to reduce the event rate with a factor of 10^3. This is done mainly by triggering on high-p_{T} objects like electrons, photons, muons and jets. By triggering on large missing E_{T} neutrinos and not yet discovered particles, for instance supersymmetric particles that do not leave a trace

[5]The first three years of operation, a peak luminosity of $2 \cdot 10^{33}$ cm^{-2}s^{-1} is expected. This is often referred to as the 'low' or 'initial' luminosity.

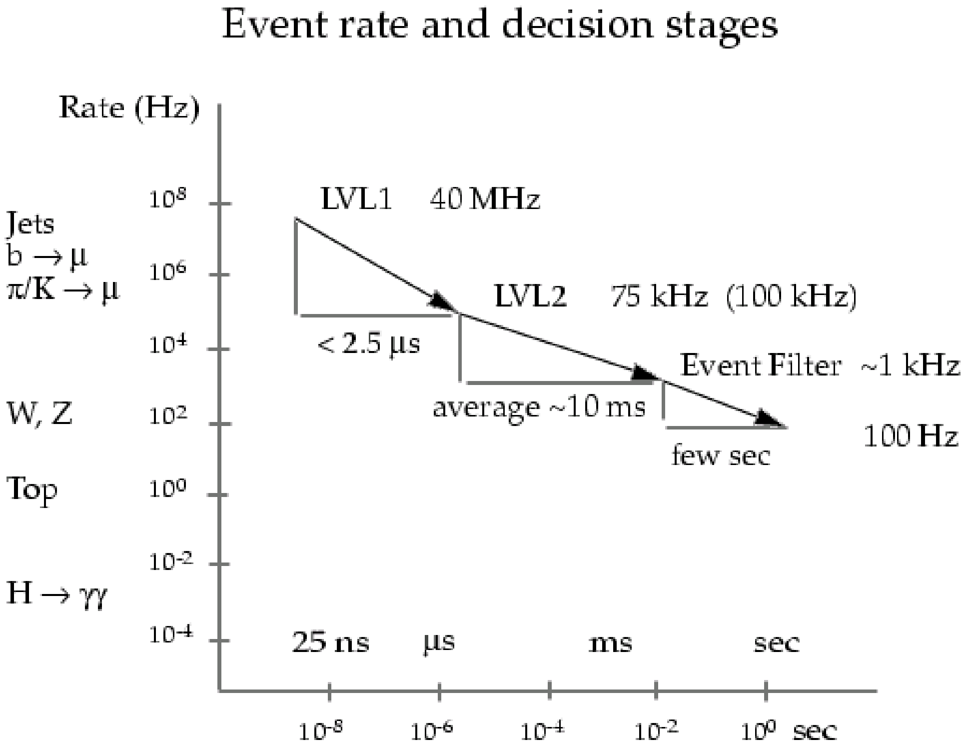

Figure 5: *The different trigger levels in ATLAS and their event rate and processing times [6].*

in the detector, are also taken into account. Since the LVL1 trigger has to operate at a very high frequency, only reduced granularity information from the calorimeters and the muon detectors is available. When an event is selected, the information in the detectors is stored in readout buffers and a 'region of interest' (RoI) is built. These RoIs are nothing more than information packages essentially containing the η, ϕ and p_{T} of interesting objects appearing in the detector. The RoIs can be classified according to in which detector the energy was deposited. A cluster in the EM calorimeter gives a 'EM RoI', a cluster in the hadronic calorimeter results in a 'jet RoI' and a track segment in the muon trigger chambers give a 'muon RoI' [10].

The input to next trigger level, LVL2, is limited to 75 kHz, which then has to be reduced to a rate around 1 kHz. At this stage, an average processing time of 10 ms is allowed. The LVL2-specific software trigger algorithms running on a farm of commodity computers have access to full granularity measurements from the subdetectors. This gives a possibility to confirm the RoIs from LVL1. When this is done, a track reconstruction commences. There are two ways of doing this:

- A *Full-scan* of the inner detector, reconstructing all the tracks.
- A *RoI-guided scan* of the inner detector, just reconstructing tracks in a limited

volume around each of the RoIs.

Different aspects of these two methods will be discussed in section 2.4.1.
By applying appropriate cuts to the tracks the amount of tracks from background events can be reduced. By combining the remaining tracks into pairs and calculating the invariant mass of these pairs, a further rejection of background events can be achieved. These steps will be described in more detail in sections 2.4.7 to 2.4.8.

The last step of the trigger, the EF accepts a input rate of about 1 kHz. A processing time of several seconds is acceptable, under which several more advanced trigger features can be used, such as bremsstrahlung recovery and common vertex fitting. Furthermore, the EF utilizes offline algorithms (i.e. the same algorithms used in the offline physics analysis) to refine the LVL2 track reconstruction, thus allowing tighter mass cuts. The events that pass the EF are stored on mass storage for later offline analysis.
An event will pass the trigger if it matches the signature of one of the interesting decays. Every decay has its own signature, or *trigger item*, which can be found in the *trigger menu*. The trigger will, at each *pp*-collision, scan the detector for trigger items on the trigger menu.

The trigger items associated with B-physics together constitute the *B-trigger*. The B-trigger must be able to identify a big variety of B-decays, while rejecting vast amounts of non-$b\bar{b}$ events and uninteresting $b\bar{b}$-events. The aim of the B-physics programme is not only to make sensitive measurements of the $\mathrm{B_d^0}$ decays, but also to measure CP-violation in all kinds of $\mathrm{B_s}$ decays. Since high statistics are required for precision measurements, it is important that the B-trigger in an efficient way can discard background events while allowing as many signal events[6] as possible to be stored for later analysis. This is also important in the search for rare B-decays, e.g. $B_{d,s} \to \mu\mu X$, that are strongly suppressed in the Standard Model and can indicate new physics if found. More on this subject can be found in [11].

2.3 The trigger simulation

The trigger has to be ready and operational when LHC starts its run in 2007. To design the trigger in forehand one has to rely on simulated data. By simulating the collisions, the detector layout and the detector response a situation as close to the realistic as possible is created. A calorimeter cluster at LVL1 does not contain as precise data as the EF, due to the small latency. To simulate this, every step of the trigger simulation uses level specific software to get realistic output. Previous work on the trigger have been done using a FORTRAN based simulation (a so called 'fast simulation'). The trigger simulations on ATLAS are now C++ based and the work is ongoing to incorporate all the different simulations into the Athena Framework[12]. To evaluate the trigger properly a complete set of trigger parts has to be simulated.

2.3.1 LVL1 clustering

When studying the trigger efficiency of $\mathrm{B_d^0} \to \mathrm{J}/\psi(e^+e^-)\mathrm{K_s}$ at LVL1, the response of the electromagnetic calorimeters needs to be simulated, among other things. The

[6] The term *signal event* refers the an event where the particular decay of interest has occurred.

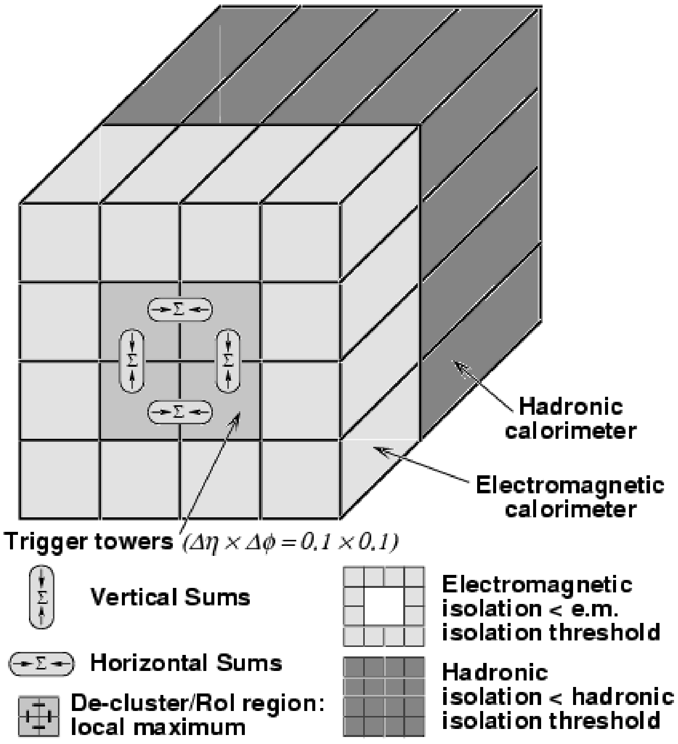

Figure 6: *A region of* 4×4 *trigger towers in the calorimeter. The lightest area is the EM calorimeter and the darkest is the hadron calorimeter. Trigger towers are formed by summing up the* E_{T} *in a quadratic region of calorimeter cells. Towers from the EM and hadronic calorimeter are formed separately and are then summed in sets of* 2×2 *towers to form RoIs. Isolation cuts are applied by summing the* E_{T} *of the EM towers around the centre and the hadronic towers behind the calorimeter.*

package TrigT1Calo[13], simulates the clustering algorithms at LVL1. The input to TrigT1Calo is a set of 'trigger towers' of size $\Delta\eta \times \Delta\phi = 0.1 \times 0.1$. Each trigger tower is a set of calorimeter cells whose energy has been added, Fig. 6 shows a region of 4×4 trigger towers. To form a cluster, TrigT1Calo forms the sum over all the 2×2 tower areas in the 4×4 tower region. The 2×2 region with the highest local E_{T}-sum will become an EM RoI if it passes an E_{T}-cut and two isolation cuts — the summed E_{T} in the isolation regions marked in Fig. 6 has to be below certain thresholds. The cluster is then classified as an EM RoI and passed on to LVL2[7]. The centre of the four towers is taken to be the position of the RoI.
Since a RoI is defined by its energy in a $\Delta\eta \times \Delta\phi = 0.2 \times 0.2$ region this sets the spatial resolution of LVL1. It is important at this point to understand the difference between this predefined resolution of an RoI in the EM calorimeter and the concept of a variable RoI size in the ID that will be used extensively in the thesis. When talking about RoI size it is *not* the size of the tower region in Fig. 6 but the size of a rectangle in the $\eta\phi$-plane centred around the RoI position, see Fig. 7. The size of

[7] This is a simplified picture of the process. For details see the ATLAS LVL1 TDR[10].

the RoI defines the regions in which a RoI-guided track search will be performed. By varying the RoI size one varies the size of the region that should be searched. See more about this in Sec. 2.4.5.

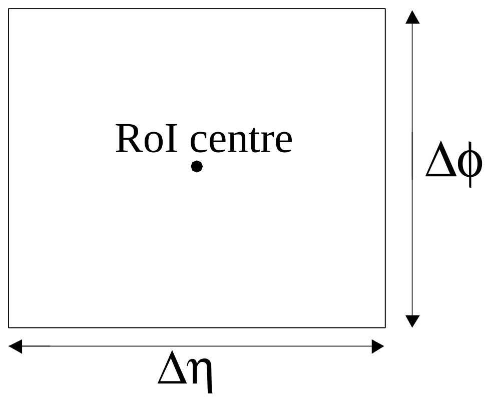

Figure 7: *The RoI size is the size of a rectangle in the $\eta\phi$-plane centred around the RoI position. It is used to limit the region needed for track reconstruction in a RoI-guided trigger.*

2.3.2 HLT algorithms

At LVL2 the RoIs from LVL1 are refined using the T2Calo package, briefly described with the other HLT algorithms in Ref. [14]. For LVL2 tracking, several packages exist. The initial intent of this study was to use the track reconstruction package IDSCAN, with an algorithm based on the Pixel and SCT detectors. Unfortunately, problems with the ATLAS software have precluded this option. At the time of writing no well-functioning LVL2 track reconstruction could be performed on the B-physics datasets relevant for this analysis. Due to this, the parts of the analysis depending on tracks will not be completely authentic. As an alternative to IDSCAN the offline reconstruction algorithm xKalman (based on the TRT, SCT and Pixel detectors) has been used. xKalman is one of the algorithms used in the next trigger level, the EF. In performance studies of the high level electron trigger comparisons between the two algorithms have been done for high-p_{T} electrons (p_{T}>20 GeV) showing a not perfect but good agreement between IDSCAN and xKalman track parameters [15]. The agreement seems to be better at low luminosities, which is the scenario the B-trigger will operate in. For low-p_{T} electrons like the ones in this thesis ($p_{\mathrm{T}} \approx 5$GeV), no similar study is available. It is therefore harder to draw any conclusions but one might guess that the agreement worsens since the curvature of the tracks becomes bigger for low-p_{T} electrons, making it harder to reconstruct the tracks exactly.
Being intended for offline use, the track reconstruction quality of xKalman is expected to be somewhat better and more precise than IDSCAN. Using xKalman in this analysis degrades the authenticity of the results, but the figures and efficiencies obtained can at least be treated as some kind of upper limit, a best case scenario.

To estimate the efficiency of the trigger it is important to study the effect of the trigger on various possible background processes. A recent change of detector layout in the detector simulation have caused compatibility problems with the trigger simulation software with the result that the available simulated background datasets cannot be processed with the LVL2 software. Due to this, no refined RoIs from T2Calo can be used. To solve this problem, offline clusters generated by the CaloRec package have been used. As in the case of the tracking, the offline clusters are 'better' than the the clusters from T2Calo. In the same high-p_{T} study as referred to above, the differences in ϕ and η were shown to be small between the offline and T2Calo RoIs. Although some differences exist in E_{T}-measurement the conclusion of the study is that the agreement is good.
The lack of LVL2 clusters have caused that in the cases where a comparison between signal and background datasets is needed, offline clusters and tracks have been used instead. This primarily concerns the plots and tables in Sec. 2.4.9. In other parts of the study, where only a signal dataset is included, LVL2 clusters have been used. To avoid ambiguities, it will be explicitly states whether offline or LVL2 clusters have been used for plots that are based on clusters.

2.4 The trigger of $\mathrm{B_d^0} \rightarrow \mathrm{J}/\psi(e^+e^-)\mathrm{K_s}$

2.4.1 The current situation

Trigger studies of $\mathrm{B_d^0} \rightarrow \mathrm{J}/\psi(e^+e^-)\mathrm{K_s}$ have been carried out before, for instance see [16]. Those studies follow the strategy outlined in Ref. [17], a strategy based on the full-scan method mentioned in section 2.2. In the full-scan the entire volume of the Inner Detector is scanned for tracks at LVL2, regardless of the existence of LVL1 RoIs. This method has proved to give good trigger efficiencies. The biggest disadvantage of the method is that it requires big resources in terms of computing power. In order for the trigger to operate within the time limits set by the latency, many processors will be needed handle the great resource demand. Recent developments have led to a situation where the B-trigger has to be altered. A new initial luminosity of $2 \cdot 10^{33}$ cm^{-2}s^{-1}, double that quoted in Ref. [17] in combination with tighter financial constraints for the HLT and the likelihood of a reduced detector at start-up [18] has led to a new strategy, outlined in [19].

In the new strategy, the ID full-scan is replaced by a RoI-guided scan. Just as the name suggests, the LVL1 RoIs are used to determine in which part of the ID a track reconstruction should be done. If the mean number of RoIs in the events and the RoI size is small, a recent study [20] estimates that the need for resources can be decreased significantly with this strategy. Furthermore, preliminary studies show that the EM RoI multiplicity (i.e. the number of RoIs from the EM calorimeter) in background processes to $\mathrm{B_d^0} \rightarrow \mathrm{J}/\psi(e^+e^-)\mathrm{K_s}$ is low enough to indicate that this new strategy *"has the potential to provide a viable alternative to the Inner Detector full-scan, requiring significantly lower resources"[18].*

2.4.2 Initiating the B-trigger

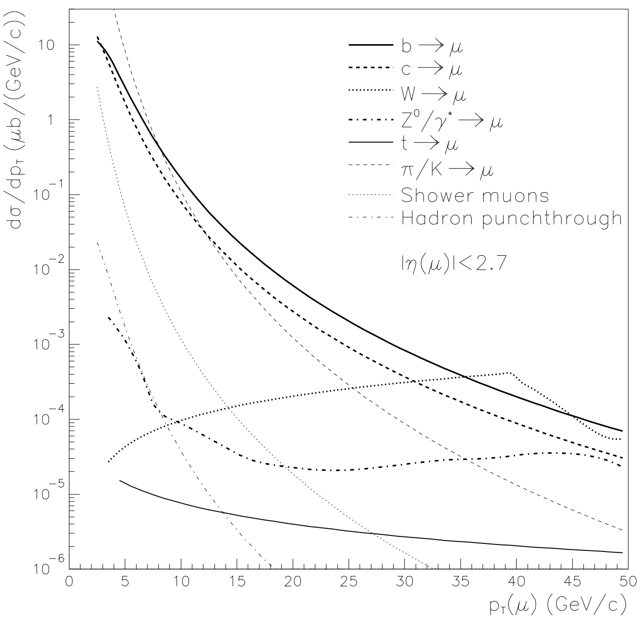

Figure 8: *The differential cross-section $d\sigma/dp_{\mathrm{T}}$ for inclusive muon production at LHC. The cross-section for $\pi/\mathrm{K} \rightarrow \mu$ dominates at low p_{T} but drops quickly with increasing p_{T}. For $p_{\mathrm{T}} \geq 8$ GeV $b \rightarrow \mu$ dominates. [21]*

In all B-decays, at least one muon in LVL1 is required to initiate the B-trigger. This muon sometimes comes from the direct decay of one of b-quarks and it provides a clear tag that makes the event easy to separate from other events. It is desired that only muons from B-decays initiate the B-trigger. Therefore the ability to discard other muons is necessary at the trigger level. Examples of possible background processes mimicking $b \rightarrow \mu$ are $c \rightarrow \mu$, $W \rightarrow \mu$ and $\pi/\mathrm{K} \rightarrow \mu$. Simulation studies of the muon cross-section at LHC show that muons from in-flight π/K-decays are by far the most common at low p_{T}-values [21]. With an appropriately set p_{T}-cut the fraction of muons that come from B-events can be increased significantly due to the quickly falling cross-section of $\pi/\mathrm{K} \rightarrow \mu$ at increasing p_{T}-values. Fig. 8 summarizes the situation. A p_{T}-cut at 8 GeV would discard many of the background muons. The drawback of setting a high p_{T}-cut is that too many good B-events will not pass the trigger. To avoid this, $p_{\mathrm{T}} \geq 6$ GeV has been used in the past. Apart from the p_{T}-cut, the muons from in-flight π/K-decays can be rejected at LVL2 when the LVL1 muon is confirmed. This is done by searching for a track in the ID that can be fitted to the muon in the muon chambers. If a track in the ID is not found, or if there appears to be a 'kink' in the trajectory, or if the origin of the track is not very close to the collision point it is highly likely that it is not a muon from a B-decay.

Although it is discussed in the recently published HLT Technical Design Report [19] whether $p_{\mathrm{T}} \geq 8$ GeV should be used instead, this analysis is based on $p_{\mathrm{T}} \geq 6$ GeV. Since no simulation of the LVL1 muon trigger simulation was available at the time of the study truth information about the muons was used.

There is another use of the muon too: in the decays of neutral hadrons to CP eigenstates, for example when the decay products are $J/\psi\ K_s$ one cannot tell if B_d^0 (with a $\bar{b}$) or $\overline{B_d^0}$ (with a b) was the mother by looking directly at the final state particles (both B_d^0 and $\overline{B_d^0}$ can decay to $J/\psi\ K_s$). Since quarks are produced in pairs in pp-collision the decay of the other b-quarks can be used to deduce tag the flavour of the b-quark in the $J/\psi K_s$ decay. If the other b-quark decays to a muon, the charge of that muon can be used. This technique is called the *muon opposite side tag*[22].

2.4.3 Trigger efficiency

As background processes the following will be considered:

- $b\bar{b}$-decays with at least one muon in the final state, $b\bar{b} \to \mu X$.
- One of the final state muons has to fulfill $|\eta| \leq 2.4$. This is a limit set by the detector geometry.
- The same muon has to fulfill $p_{\mathrm{T}} \geq$ 6 GeV.

The cross-section of a process that answers to all the above conditions has been calculated to be

$$\sigma(b\bar{b} \to \mu X,\ p_{\mathrm{T}}(\mu) \geq 6\ \mathrm{GeV}, |\eta| \leq 2.4) \simeq 2.3\ \mu\mathrm{b}$$

If it is assumed that all these events pass LVL1(this demands a high efficiency of the LVL1 muon trigger) and that LHC operates at an instantaneous luminosity of

$$\mathcal{L} = 2 \cdot 10^{33}\ \mathrm{cm}^{-2}\mathrm{s}^{-1} \quad ,$$

the rate of which the background events enter LVL2 can then be calculated to be:

$$R_{LVL1,bg} \equiv \frac{\mathrm{dN}(b\bar{b} \to \mu X)}{\mathrm{dt}} = \sigma \cdot \mathcal{L} = 4.6\ \mathrm{kHz} \tag{6}$$

according to Eq. 5.
Since the signal channel is included in these 4.6 kHz it is possible to estimate the cross-section for $\mathrm{B_d^0} \to \mathrm{J}/\psi(e^+e^-)\mathrm{K_s}$ by using the branching ratios:

BR($b \to J/\psi X$)$\approx$ 0.01
BR($J/\psi \to e^+e^-$)$\approx$ 0.06

The $\mathrm{K_s}$ is not included in the above since it will no be reconstructed at LVL2 but at a later stage (in the EF or the offline analysis). Instead, the focus in LVL2 is mainly on finding the electrons from J/ψ.
The cross-section for signal events of the type $\mathrm{B_d^0} \to \mathrm{J}/\psi(e^+e^-)X$ is estimated to be

$$\sigma(\mathrm{B_d^0} \to \mathrm{J}/\psi(e^+e^-)X) = \sigma(b\bar{b} \to \mu X) \cdot 0.01 \cdot 0.06 = 6.4 \cdot 10^{-4} \cdot 2.3\ \mu\mathrm{b}\ .$$

This cross-section does not contain any constraints on the p_{T} and η of the emitted electrons. But, as for the muon, some properties of the detector (e.g. geometry and the subdetectors ability to measure low p_{T}-objects) will require the introduction of such constraints. This will scale down the cross-section with a factor λ, where $0 \leq \lambda \leq 1$. Including this scale factor we can in the same way as in Eq. 6 estimate the signal event rate to be

$$R_{LVL1,signal} \equiv \frac{\mathrm{dN}(\mathrm{B_d^0} \to \mathrm{J}/\psi(e^+e^-)X)}{\mathrm{dt}} = 4.6\ \mathrm{kHz} \cdot 6.4 \cdot 10^{-4} \cdot \lambda \tag{7}$$

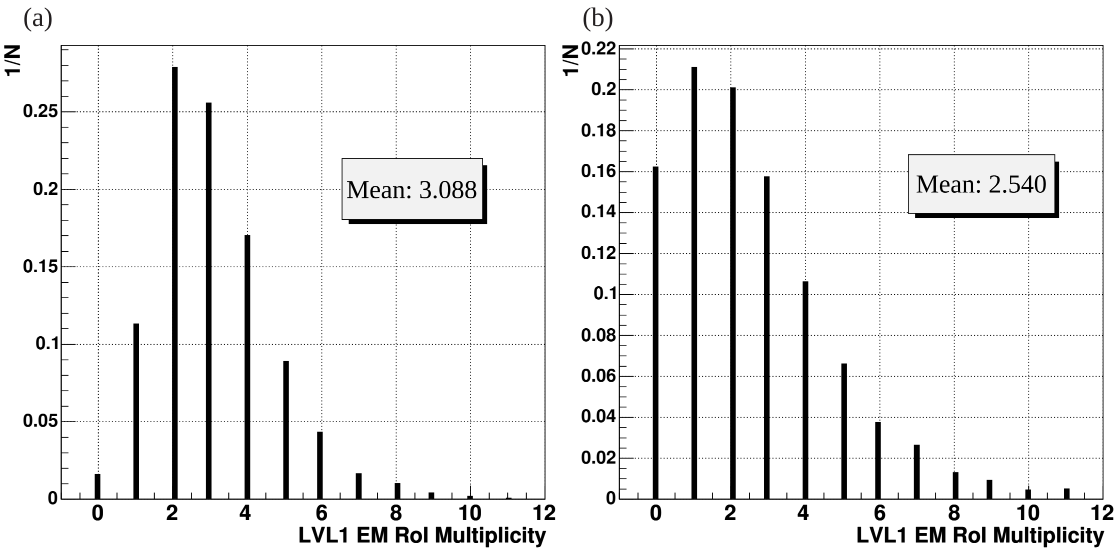

Figure 9: *LVL1 EM RoI Multiplicity for a) signal events and b) background events of type* $b\bar{b} \to \mu X$*. The histograms are normalised to the total number of events.*

Comparing the results from eq. 6 and 7 we see that that $R_{LVL1,signal} \ll R_{LVL1,bg}$ so the output from LVL1 will be totally dominated by background events of the type $b\bar{b} \to \mu X$.
We define

$$R_{LVL2,bg} \equiv \varepsilon_{bg} \cdot R_{LVL1,bg} \qquad \text{and} \qquad R_{LVL2,signal} \equiv \varepsilon_{signal} \cdot R_{LVL1,signal} \quad ,$$

where ε_{signal} is the *LVL2 trigger efficiency*. It is taken to be the number of signal events that pass all the LVL2 trigger cuts, normalised to the total number of signal events that passed LVL1. Analogously ε_{bg} is the trigger efficiency for background events. The challenge for the LVL2 trigger is to minimise ε_{bg} while maximising ε_{signal}.

The old trigger strategy, and thus the old trigger studies, were based on a total LVL2 B-physics bandwidth of about 840 Hz, where the trigger of $\mathrm{B}_\mathrm{d}^0 \to \mathrm{J}/\psi(e^+e^-)$ was allocated 310 Hz of this bandwidth. In light of the changes of the B-programme (as discussed in sec. 2.4.1), the bandwidth of this channel has been reduced to 10 Hz [19]. This places new demands on the trigger. It may not be possible to keep the high trigger efficiencies of about 50% that are quoted in [16]. Following the new bandwidth directives, an upper limit on ε_{bg} can be set. Allowing R_{LVL2} =10 Hz and assuming that $R_{LVL2,bg}$ will dominate the bandwidth the background efficiency should suppressed to an order of $\varepsilon_{bg} \approx 0.2\%$.

2.4.4 RoI multiplicity

The LVL2 trigger seeks to identify and reconstruct the two electrons from the J/ψ-decay. Following this, a first condition for an event to pass LVL2 should be the presence of two or more EM RoIs. These RoIs also should pass an E_T-cut of $E_\mathrm{T} \geq 2$ GeV, to sort out RoIs coming from contaminating pile-up events[8]. If too few EM

[8]Pile-up events were explained in Sec. 2.2.

clusters are detected the LVL2 signal efficiency drops a lot compared to the full-scan. A look at Fig. 9a shows that this is not the case. Instead, we see that in only about 2% of the signal events no EM RoI was found at LVL1. If two RoIs are required then about 13% of the events are rejected immediately at LVL2.
Another important aspect of the RoI-guided trigger is the RoI multiplicity in background events. The higher it is, the bigger volume of the ID will be scanned for tracks. If it is too high the resources required for scanning the volume around the RoIs will be comparable to the resources needed by a full-scan. It is therefore important that the mean RoI multiplicity for background events is low. In Fig. 9b the background RoI multiplicity is plotted and as can be seen, the mean multiplicity is about 2.5. This is higher than in [18] where a mean of about 1 was found using the old FORTRAN-based trigger simulation. The inconsistency is interesting and worth looking further into. It is not within the scope of this study though.

2.4.5 RoI size

For an efficient RoI-guidance it is important that the electrons can be found inside the RoIs. Often, the RoIs from LVL1 are not caused by electrons. Instead, for instance, a pion can cause a cluster in the ECAL, giving an EM RoI. In Fig. 10a the size of the RoI (as defined in Fig. 7 but using a quadratic RoI, $\Delta\eta = \Delta\phi$) is plotted versus the efficiency to find both electrons. The efficiency is taken to be the fraction of events with two or more RoIs where the electrons are located in different RoIs. The efficiency is slowly growing with the RoI size. With a mean signal EM RoI multiplicity of about 3 (Fig. 9a) and a not negligible fraction of events with higher multiplicities, the RoI size cannot be too big. In the recent resource estimate study for the B-trigger [20], a RoI size of $\Delta\eta \times \Delta\phi = 0.2 \times 0.2$ was assumed. As can be seen, the efficiency for finding both electrons at this size about 40%. By requiring at least two RoIs 87% of the events would make the cut(see Fig. 9a). Of these 87% both electrons can be found in 40% of the events. This limits the maximum efficiency to 35% (40% of 87%).

To raise the efficiency events with one RoI in LVL1 can also be included. Fig. 10b shows the efficiency to find both electrons in a single RoI versus the RoI size. Note that only events with one RoI are included in this plot. Apparently, a big RoI is needed to achieve good results. Since these events only have one RoI the RoI is allowed to be bigger than in the multiple RoI events. A RoI with a side of 2.5 would be enough to pinpoint both electrons in about 75 % of the events. The single RoI events represent 11% of the the total events sample. The 75% of these events where both electrons can be found give a rather small contribution to the total efficiency compared to the loss in background rejection that is the result of including single RoI events. Fig. 9b shows that the single RoI events are 21% of all background events. This is one of the drawbacks with using single RoI events. Another way to improve the efficiency without including single RoI events would be to increase the RoI size. A size of $\Delta\eta = \Delta\phi = 0.8$ would give an efficiency of 60%. If the RoI size is increased more, the efficiency rises but the resource load is also increased. As a measure of the load one can take a look how big fraction of the ID that would have to be scanned for tracks at different RoI sizes.
The region of the ID that can be scanned for tracks is limited by the detector

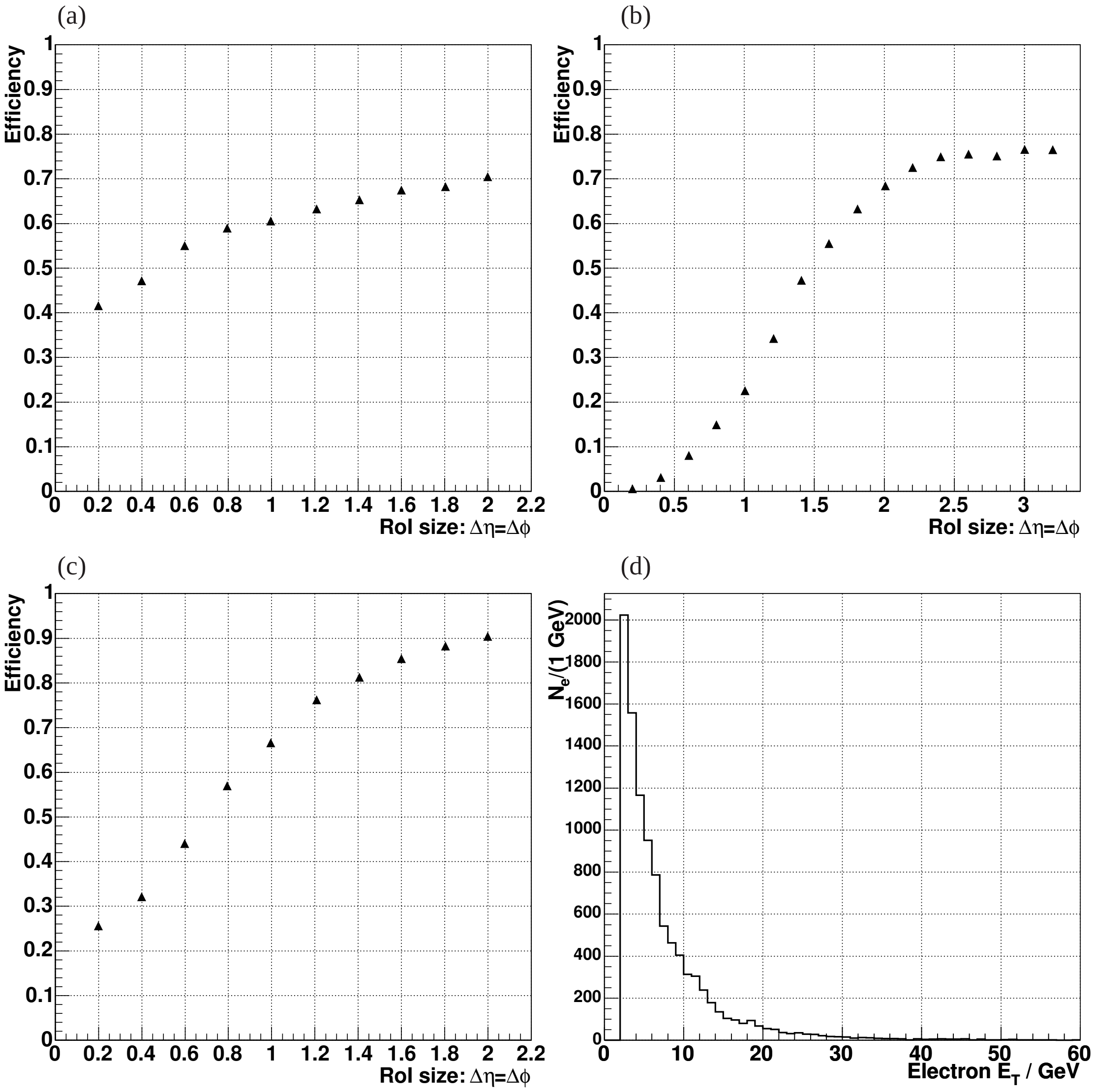

Figure 10:
The efficiency to find both electrons in
a) different RoIs in events with two or more RoIs.
b) the same RoI in events with a single RoI.
c) in the same RoI in events with two or more RoIs.
d) The E_{T}*spectrum of the electrons in* $\mathrm{B}_{\mathrm{d}}^0 \rightarrow \mathrm{J}/\psi(e^+e^-)$.

geometry to $|\eta| \leq 2.5$ and $|\phi| \leq \pi$, corresponding to a area of 10π in the $\eta\phi$-plane. A RoI that is quadratic in the $\eta\phi$-plane with the length 2 would then make up

$$\frac{2 \cdot 2}{10\pi} \approx 0.13 \qquad (13\%)$$

of the total area. But, one must not forget that η depends non-linearly on θ (according to Eq.2). Therefore, the actual fraction will vary depending on the location of the RoI in the ID. The fraction has its maximum when the RoI has its centre at $\theta = 0$. At the maximum point the same RoI as above would make up about 20% of the total ID acceptance. This value drops quickly as θ increases though. The same RoI with its centre at $\theta = 40°$ would only constitute about 7% of the total ID area. In some sense the $\eta\phi$-plane can then be treated as some kind of average when estimating the resources needed for a certain RoI size.

In Fig. 10a the efficiency to find the electrons in *different* RoIs was plotted. When a track reconstruction has been performed in the RoI, tracks from different RoIs are combined and their invariant mass is calculated. To increase the efficiency tracks from the *same* RoI can also be combined. This increases the amount of combinations involved in a trigger decision resulting in a bigger probability for background events to be accepted. But, by allowing all track combinations there is a bigger chance that both the electron tracks are found. In Fig. 10c the efficiency to find both electrons in the same RoI is plotted, for events with RoI multiplicity greater than 2. Comparing 10a with 10c it can be seen that the curves coincide around $\Delta\eta = \Delta\phi = 0.8$. When going above that size, the efficiency increases quickly in Fig. 10c , at a size of 1.4 it is about 80%. A RoI of this size corresponds to about 6.5 % of the ID acceptance. If this size is feasible from a resource point of view it provides a way to raise efficiency for finding electrons from $\mathrm{B_d^0} \rightarrow \mathrm{J}/\psi(e^+e^-)$.

2.4.6 Downscaled full-scan or 'true' RoI-guidance?

To decide which RoI size is preferable a question of trigger philosophy might be raised. Should the trigger work as a downscaled full-scan trigger or as a 'true' RoI-guided trigger? In a true RoI-guided trigger the aim of the RoI-guidance is to match an electron track to its corresponding EM cluster. In this scenario, the RoI size should be small(e.g. $\Delta\eta \times \Delta\phi = 0.2 \times 0.2$) in order to sort out irrelevant tracks and raise the probability for a correct match. The downscaled full-scan trigger instead acts as if it were a full-scan trigger, the difference being scanning a smaller part of the ID. In this scenario it is not only accepted but also exploited that although there is a big chance to find an electron track very close to an EM cluster, many of the electrons are not associated with RoIs and therefore a big RoI size is needed to find both electrons. In this method it is of less importance to try to match tracks to clusters. As will be seen in Sec. 2.4.7, track matching proves to be a good way of sorting out non-electron tracks.

Looking at the plots in Fig. 10 its not at all obvious in which manner the trigger should work. For small RoI sizes the probability to find both electrons in the RoIs is about 40 %. In a great deal of events only one or none of the EM RoIs are connected to an electron. The reasons for this might be that the clustering algorithms are optimized to work with more high-E_{T} objects than the electrons in $\mathrm{B_d^0} \rightarrow \mathrm{J}/\psi(e^+e^-)$. Fig. 10d shows the E_{T}-spectrum of these electrons. A big fraction of the electrons have transverse energies of just a few GeVs.
To summarise the situation: a true RoI-guided trigger will lose a lot of good events but a downscaled full-scale will introduce a lot of non-electron tracks that are hard to sort out.

2.4.7 Track matching

So far the events that have passed the cuts fulfill:

- One muon with $|\eta| \leq 2.4$, $p_{\mathrm{T}} \geq 6$ GeV.
- At least two EM RoIs with $E_{\mathrm{T}} \geq 2$ GeV.

The next step is to match tracks to these RoIs. For every RoI there will be a set of tracks aspiring to be the right track. The track multiplicity depends on the RoI size (Fig. 11). The strength of a true RoI-guided trigger lies in its ability to efficiently match electron tracks with their clusters. In Fig. 11 we see that already the smallest RoI size in the plot gives a mean track multiplicity of 3 tracks per RoI. A RoI size of 1.0×1.0 gives a mean of 12 tracks/RoI. Since the RoIs can overlap tracks can be shared between the RoIs so the number of unique tracks/RoI is not that big. When the invariant mass of different track combinations is calculated at a later stage, only unique track combinations will be used so a big track multiplicity does not automatically mean many possible track combinations.

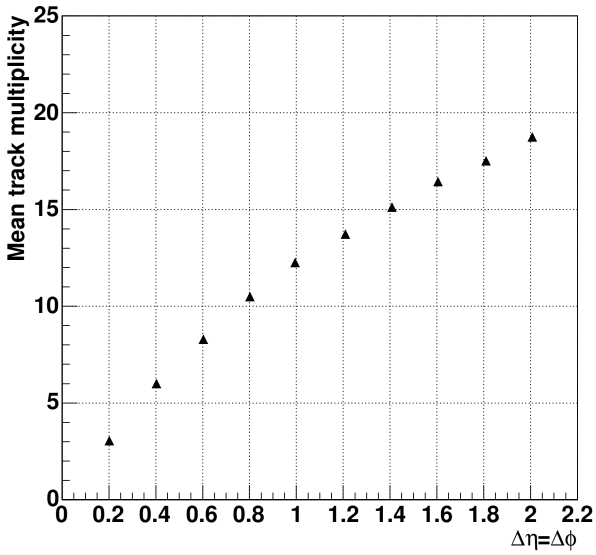

Figure 11: *The mean track multiplicity per RoI at different RoI sizes. LVL2-RoIs have been used.*

The electrons at LHC have a small mass compared to their kinetic energy so they can be considered massless. Furthermore, the electromagnetic calorimeter is designed so that the electrons should deposit all their energy in it. Therefore we expect that $(E_{\mathrm{T}})_{cal} \approx (p_{\mathrm{T}})_{track}$ or $E_{\mathrm{T}}/p_{\mathrm{T}} \approx 1$. This is used to match clusters to tracks and also to find electron tracks. The calorimeter delivers the energy and the track delivers the momentum. By scanning the EM RoIs for tracks in each event and dividing the RoI energy with the momentum of the track, plot Fig. 12a was made. The RoI size was $\Delta\eta \times \Delta\phi = 0.2 \times 0.2$. The solid line shows that for electrons tracks a peak at 1 can be seen as predicted. The right tail is due to bremsstrahlung of the electrons. If a bremsstrahlung photon is not too hard, its trajectory will be close the the electron trajectory. When it hits the ECAL it will deposit its energy very close to the electron resulting in a RoI with the energy of the electron before the photon emission. Since the track on the other hand is based purely on the electron, only the electron p_{T} will be measured. The $E_{\mathrm{T}}/p_{\mathrm{T}}$-ratio then becomes shifted to higher values. The strong peak at 1 also indicates that when an electron track is found within an RoI, in most cases the electron was the particle to cause the EM cluster. Whenever the ratio is taken between an electron track and a cluster originating from another particle, E_{T} and p_{T} will not coincide at all, something that can be seen in the plot as some few events all the way up to $E_{\mathrm{T}}/p_{\mathrm{T}} = 4$. The dashed line shows $E_{\mathrm{T}}/p_{\mathrm{T}}$ for all tracks not coming from electrons. In the cases where the particle causing the track was not the same as the particle causing the cluster, any value can be assumed in $E_{\mathrm{T}}/p_{\mathrm{T}}$-spectrum. A part of the peak at 0.5 is associated tracks that match the cluster but come from hadrons like pions and kaons that deposit some part of their energy in the EM calorimeter and the rest in the hadronic calorimeter.

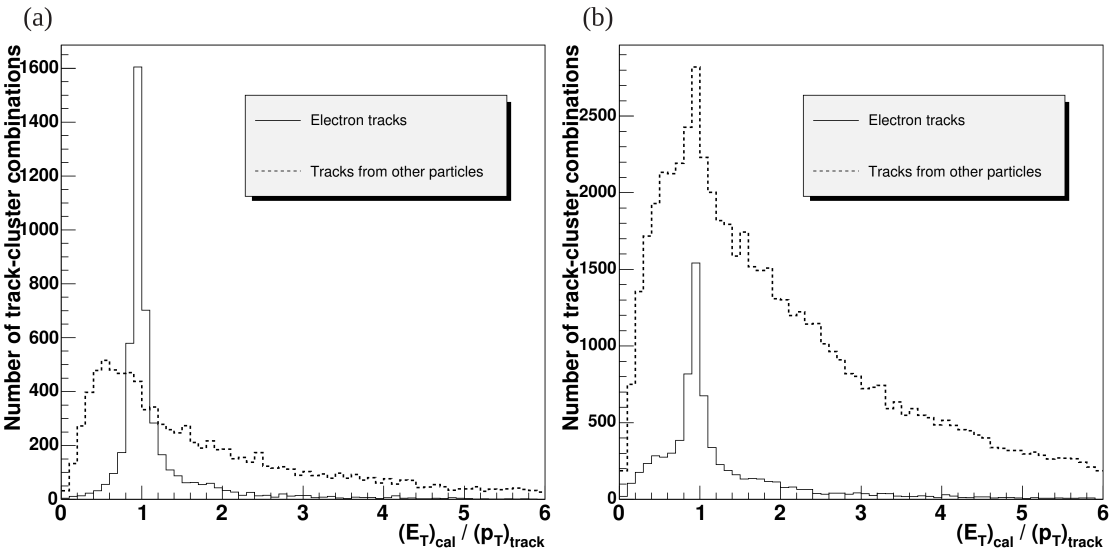

Figure 12: $(E_{\mathrm{T}})_{cal}/(p_{\mathrm{T}})_{track}$ *for tracks from electrons(solid line) and other particles (dashed line) for a RoI of dimensions*
a) $\Delta\eta \times \Delta\phi = 0.2 \times 0.2$
b) $\Delta\eta \times \Delta\phi = 1.4 \times 1.4$
LVL2 clusters were used.

To reject non-electron tracks, an $E_{\mathrm{T}}/p_{\mathrm{T}}$-cut can be applied. In this example, a cut at $0.7 \leq E_{\mathrm{T}}/p_{\mathrm{T}} \leq 1.4$ would reduce the number of non-electron tracks by 72% while keeping 80% of the electron tracks. In the downscaled full-scan trigger cut like this would not give the same powerful rejection of non-electron tracks. Fig. 12b shows the situation at a RoI size of 1.4×1.4. The peak at 1 for the electrons remains but the big RoI size increases the amount of background tracks significantly. The amount of electron tracks (the area under the solid line) increases with almost a factor 2 but these extra tracks are distributed over a big $E_{\mathrm{T}}/p_{\mathrm{T}}$-range. To benefit from the the increased amount of electron tracks very a loose $E_{\mathrm{T}}/p_{\mathrm{T}}$-cut is needed. For instance, a cut at $0.2 \leq E_{\mathrm{T}}/p_{\mathrm{T}} \leq 1.4$ increases the number of electron tracks with a factor of 1.5 compared to the small RoI case, but the number of non-electron tracks with a factor of 8.5. To decrease this huge amount of non-electron tracks in LVL2 new cuts have to be applied, e.g finding a common vertex for two tracks and apply a cut on the distance from vertex to the interaction point or utilizing TRT electron identification. These cuts are time consuming and therefore not suitable in LVL2 at the current resource situation.
Due to this, the 'true' RoI-guided trigger is recommended. The good possibilities to match electron tracks to clusters successfully without including too many non-electron tracks are promising.

2.4.8 Cuts on track combinations

To calculate the invariant mass of the tracks they are combined in pairs. To reject combinations without two electron-tracks additional cuts can be applied. The $E_{\mathrm{T}}/p_{\mathrm{T}}$-cut drastically decreased the number of non-electron tracks, but a RoI can still be associated with more than one track. By forming pairs of tracks from different RoIs, a collection of track combinations is created. If two RoIs overlap there is a possibility for them to share tracks. It is important to account for this when the track combinations are formed. Each track combination in an event must be unique and a track present in two RoIs must not be combined with itself.

The first cut that can be applied is to demand that the tracks have different charge This is an obvious demand since the an electron and a positron are emitted from a J/ψ. Next, a p_T-cut can be applied. Instead of allowing a minimum p_T for each track, the sum of the p_T-value of the two tracks is required to be above a certain level instead. Although an E_T-cut was applied to the RoIs in an earlier stage of the trigger, the tracks can have a lower p_T. This is a consequence of including tracks with $E_T/p_T < 1$. The signal dataset used in this analysis only contains electrons with a generated $p_T \geq 2$ GeV but since some energy is lost due to bremsstrahlung the tracks can be have a lower momentum and energy. The plot in Fig. 13 shows the p_T-sum for electron track combinations and other track combinations(i.e where at least one of the tracks is a non-electron track). A cut at $|p_{T1}| + |p_{T2}| \geq 5$ would decrease some of the background without rejecting much of the signal. As can be seen, the effect of this cut is not big though.

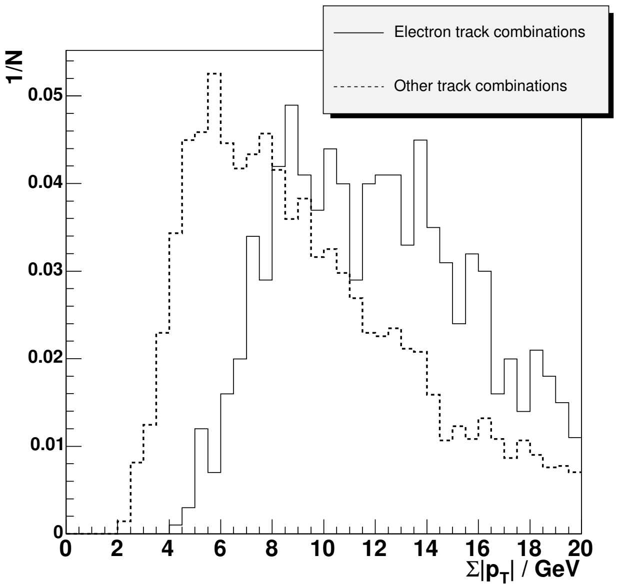

Figure 13: *A plot of* $|\mathrm{p_{T1}}| + |\mathrm{p_{T2}}|$ *for electron track combinations(solid) and combination where at least one of the tracks is a non-electron track.*

The electrons from $\mathrm{B_d^0} \rightarrow \mathrm{J}/\psi(e^+e^-)\mathrm{K_s}$ will be emitted within certain angles relative to each other. The difference in emitted η and ϕ between the electrons in the signal dataset is plotted in Fig. 14. By combining $\Delta\eta_{1-2}$ and $\Delta\phi_{1-2}$ to ΔR, defined by Eq. 3 the distance between two tracks in the $\eta\phi$-space can be plotted, see Fig. 15. The track combinations with two electrons are almost exclusively emitted with $\Delta R < 1$. By applying such a cut the majority of the other types of track combinations are rejected.

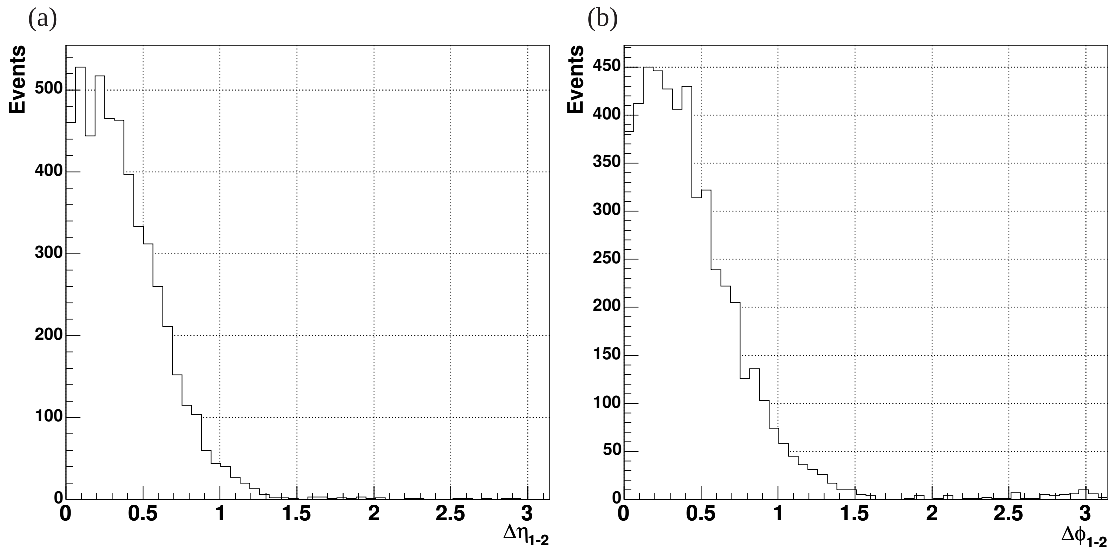

Figure 14: *The distance between the two electrons in a) pseudorapidity η and b) azimuthal angle ϕ*

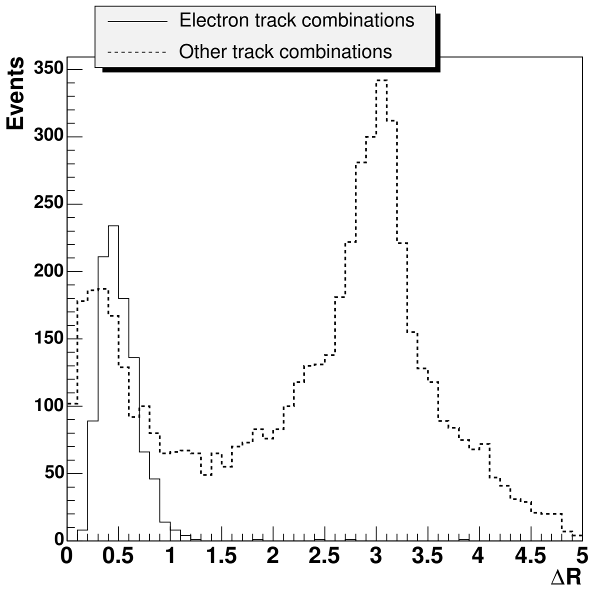

Figure 15: $\Delta R = \sqrt{(\Delta\eta)^2 + (\Delta\phi)^2}$ *between tracks. The solid line shows ΔR between J/ψ-electrons and the dotted line shows ΔR between tracks from other particles.*

Fig. 14 also provides another interesting piece of information, it explains the behaviour of Fig. 10b where the efficiency to find both electrons in a single RoI was plotted. If one of the electrons is located very close to the RoI centre (i.e. in the cluster) we expect the second electron to be found anywhere within a distance of $\Delta\eta_{1-2} \approx \Delta\phi_{1-2} = 1$ from the RoI centre. The maximum RoI size needed then becomes $\Delta\eta \times \Delta\phi = 2 \times 2$ manifesting itself as the plateau behaviour for sizes over 2 in fig. 10b. The efficiency is expected to grow very slowly for bigger RoI size since any increase comes from finding both electrons where none of them is matching the cluster.

2.4.9 The invariant mass cut

The invariant mass of two tracks can be calculated according to Eq. 4. Many of the events may still be associated with more than one possible track combinations but only one combination from each event is allowed to be represented in the invariant

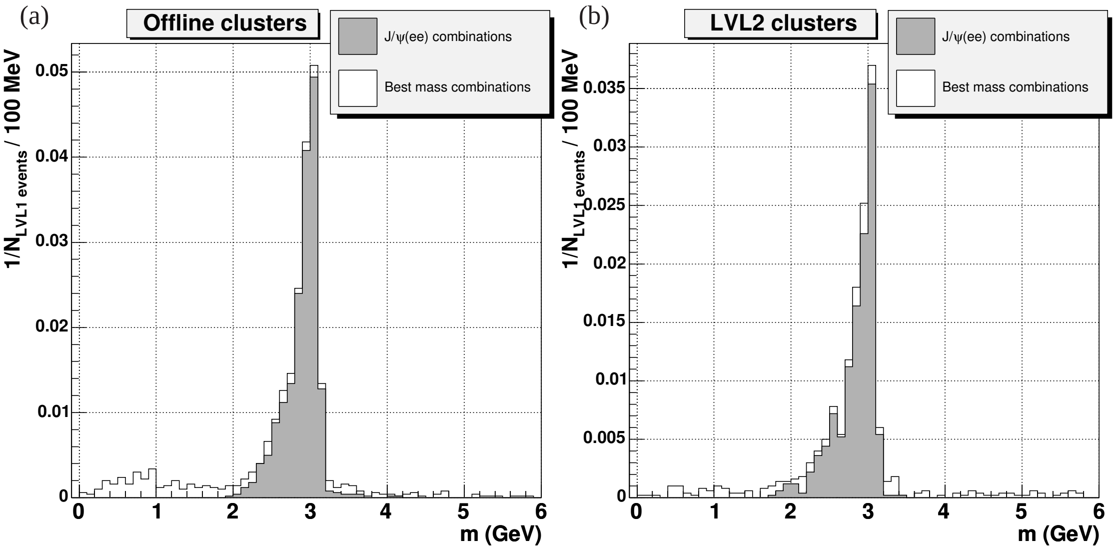

Figure 16: *Plot of the best invariant mass produced with a) offline clusters b) LVL2 clusters. Both plots are based on a RoI size of* $\Delta\eta \times \Delta\phi = 0.2 \times 0.2$ *and normalised to the number of events before any LVL2 cuts were applied. To show the purity of the plots the part of the peak that comes from two real* J/ψ*-electrons are shaded grey.*

mass plot. The selection is made by choosing the combination with a mass closest to the J/ψ nominal mass of 3.0987 GeV, here referred to as the 'best mass'. This will bias the data to peak around the J/ψ-mass so it is of no use to do a Gaussian fit on the peak obtained. The events with a track combination giving an invariant mass between 2 GeV $\leq m \leq$ 3.5 GeV are selected to pass LVL2.
Since no functioning LVL2-clustering for background datasets was available at the time of the writing, it is not possible to compare the effects of the trigger on a signal dataset versus a background dataset without using offline clusters (see discussion in Sec. 2.3.2). Table 2 shows the efficiencies obtained at each step of the trigger, in the order the cuts were applied. A comparison between signal and background for two different RoI sizes is listed, using offline algorithms. Also, the efficiency obtained from of a signal dataset with RoI size $\Delta\eta \times \Delta\phi = 0.2 \times 0.2$ using LVL2-clusters is included. Fig. 16a and b show the invariant mass for signal datasets for offline and LVL2-clusters using a $\Delta\eta \times \Delta\phi = 0.2 \times 0.2$ RoI size in both plots. The plots are normalised to the number of events that passed LVL1. As can be seen the purity of the peaks is high. A majority of the track combinations come from J/ψ-decays and a small fraction is due to combinatorial background. The list of cuts used are listed in Table 2.
To demand a LVL1 EM RoI multiplicity higher than 1 is an efficient way to reduce the background, as expected. The track matching condition of $0.7 \leq E_{\mathrm{T}}/p_{\mathrm{T}} < 1.4$ also reduces the background significantly. The drop in efficiency in the signal dataset when applying the track matching condition is not due to the cut but an expected result following the efficiency plot in Fig. 10a which showed that there is a upper limit on how efficiently both electrons can be found in a RoI-guided trigger. The cut on the p_{T}-sum of two tracks proves not be very useful in this case, if it had been introduced before the ΔR-cut it might have had some impact.
A RoI size of $\Delta\eta \times \Delta\phi = 0.2 \times 0.2$ ('small' RoI size) gives a signal efficiency of 18.9%

and a total background efficiency of 0.3%, in the same order of magnitude as what was estimated in Sec. 2.4.3. Increasing the RoI size to $\Delta\eta \times \Delta\phi = 0.4 \times 0.4$ ('big' RoI size) yields in an increased background efficiency(1%) but also in an increased signal efficiency (28.9%). Although offline clusters and offline tracking has been used to produce the efficiency figures in the comparison between signal and background events, one can treat the efficiencies as an approximate behaviour of the trigger. Comparing the small RoI signal efficiency for the offline and LVL2 cluster columns shows that the efficiency is lower in the more realistic case of using LVL2 clusters. It can be expected that the efficiency would drop even more if LVL2 tracks had been used. Although it is hard to say anything how low the 'real' LVL2 efficiency would be one might guess that it is about 10%. Fig. 17 shows how a increase in RoI size leads to an increase in signal efficiency when using LVL2 clusters. Since no background analysis has been made with LVL2 clusters, it is hard to evaluate how big the RoI size can be without obtaining a too big background efficiency, but reaching signal efficiencies above 30% may not be possible in a RoI-guided trigger.

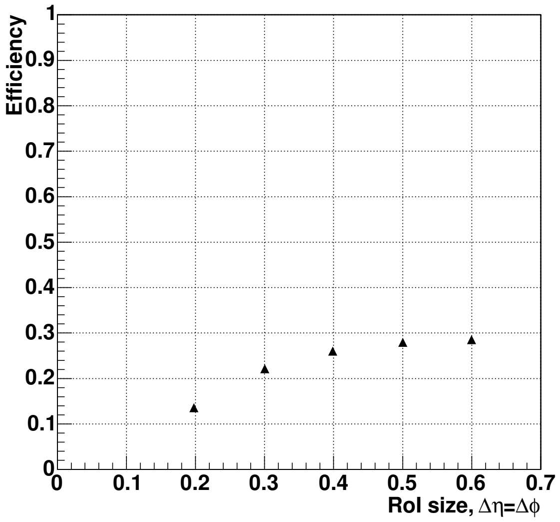

Figure 17: *The signal efficiency at different RoI sizes when using LVL2 clusters*

2.5 Conclusion

The RoI-guided trigger for $B_d^0 \to J/\psi(e^+e^-)K_s$ has been evaluated as an alternative to the current full-scan trigger. The probability of finding both electrons from J/ψ by RoI-guidance is depending on how big area around each EM cluster that is scanned for electron tracks, i.e. the RoI size. To limit the trigger rate a small RoI size needs to be chosen. This limits the probability to find both electrons in an event, setting a maximum value of the signal efficiency. For a RoI size of $\Delta\eta \times \Delta\phi = 0.2 \times 0.2$ this upper limit is about 40% in events with two or more LVL1 EM RoIs. By not including events with one RoI the a high background rejection can be obtained without reducing the signal efficiency much. By matching of tracks to clusters electron tracks can be found successfully. When additional cuts on track combinations are applied and a generous invariant mass cut of 2 GeV $\leq m \leq$

	Offline clusters				LVL2 clusters
	'Small' RoI		'Big' RoI		Small RoI
LVL2 Cut	Signal	Background	Signal	Background	Signal
$\geq$ 2 LVL1 EM RoIs	77.0	41.4	77.0	41.4	87.1
$0.7 \leq E_{\mathrm{T}}/p_{\mathrm{T}} < 1.4$	38.1	7.4	54.2	14.9	33.5
Opposite charge	30.8	4.7	45.3	10.5	23.8
$\lvert\Delta R\rvert < 1$	23.2	2.2	36.3	5.5	15.2
$\lvert \mathrm{p_{T1}}\rvert + \lvert \mathrm{p_{T2}}\rvert$	23.2	2.2	36.3	5.3	15.0
2 GeV $\leq m \leq$ 3.5 GeV	18.9	0.3	28.9	1.0	13.0
Total efficiency	18.9	0.3	28.9	1.0	13.0

Table 2: *Trigger efficiencies for each step of the trigger, listed in the order they are applied. All figures are normalised to the number of events before any cuts were applied and are listed as percentages. Small RoI means* $\Delta\eta \times \Delta\phi = 0.2 \times 0.2$ *and big RoI means* $\Delta\eta \times \Delta\phi = 0.4 \times 0.4$.

3.5 GeV is applied a LVL2 signal efficiency of the order of 10% is achieved. This estimate is based on the total efficiency of the signal sample with LVL2 clusters in Table. 2. The uncertainty in the efficiency estimate is due to the lack of access to a complete LVL2 trigger simulation. If the efficiency is raised by increasing the RoI size the strategy described in this study a upper limit of 30% still seems to exist. These efficiency figures are worse than in the case of a full-scan. Including $\mathrm{B_d^0} \rightarrow \mathrm{J}/\psi(e^+e^-)\mathrm{K_s}$ in the trigger menu is nevertheless important in order to increase the overall statistics of the $\mathrm{B_d^0} \rightarrow \mathrm{J}/\psi\mathrm{K_s}$ sample and to obtain a control sample for defining various systematic effects in the analysis of the $\mathrm{B_d^0} \rightarrow \mathrm{J}/\psi\mathrm{K_s}$ decay. It has been shown that it is feasible to design trigger cuts which keep the background rate within allowed limits.

3 Analysis on LHCb

The topics covered in this section are the result of an initial study of the use of dielectrons at the level 1 trigger of LHCb, and can also be found in Ref. [23]. Dielectrons in this case mean the electrons from the decay $\mathrm{B_d^0} \to \mathrm{J}/\psi(e^+e^-)\mathrm{K_s}$. The dimuon decay of this channel ($\mathrm{J}/\psi \to \mu^+\mu^-$) is already included in the trigger, but the efficiency of $\mathrm{B_d^0} \to \mathrm{J}/\psi\mathrm{K_s}$ would be raised by including the dielectron decay. Comparing the dimuon and dielectron decays offers an opportunity to cross check the CP-violation measurements as well. The dielectron channel is harder to reconstruct due to bremsstrahlung losses of electrons. The energy loss results in a broader J/ψ invariant mass peak than what is the case in the dimuon decay. This motivated an attempt to perform a bremsstrahlung reconstruction already at level 1. The work with the bremsstrahlung reconstruction led to the more ambitious attempt to pinpoint the electrons with an invariant mass cut, using only calorimeter clusters. This can hardly be seen as an efficient method but it offers an interesting test of the capability of the calorimeters. The ATLAS trigger study utilized both calorimetry and tracking thus giving it a more realistic framework while the LHCb trigger study should be seen as an initial study which prepares the ground for a more detailed study.

3.1 The LHCb experiment

The main difference between the LHCb detector and ATLAS is the angular coverage. LHCb is a one-arm spectrometer located at small angles around the beam pipe ($1.9 < \eta < 4.9$). In Fig.18 an overview of the LHCb spectrometer can be seen. The key subdetectors are the Vertex Locator (VELO) and the two Ring-Imaging Cherenkov detectors (RICH 1 and 2). The VELO will provide an accurate measurement of the displaced decay vertices characteristic for B-mesons while the RICH detectors are used for hadron identification. Tracking is performed in the tracking stations TT (trigger tracker) and T1-3. A calorimeter system (ECAL, HCAL) with electron/photon/hadron separation capabilities (PS,SPD[9]) is also used, together with muon chambers (M1-M5). LHCb will operate at a luminosity of $2 \cdot 10^{32}$ $\mathrm{cm^{-2}s^{-1}}$ regardless of the higher LHC luminosity. This main reason to do this is to reduce the mean multiplicity of interactions at each bunch crossing to one. To reject bunch crossings with more than one interaction, a pile-up veto can be used. Although the interaction rate is lower than in ATLAS the advantage of using single interactions is that the problem with contaminating pile-up is avoided thus simplifying the work of the trigger by giving a more clean working environment.
The right-handed coordinate system in LHCb has its origin at the interaction point and the z-axis pointing along the beam line in the direction of the detector. The magnetic field causes a particle with an initial trajectory parallel to the z-axis to be deflected in the x-direction.

[9]Preshower, Scintillating Pad Detector.

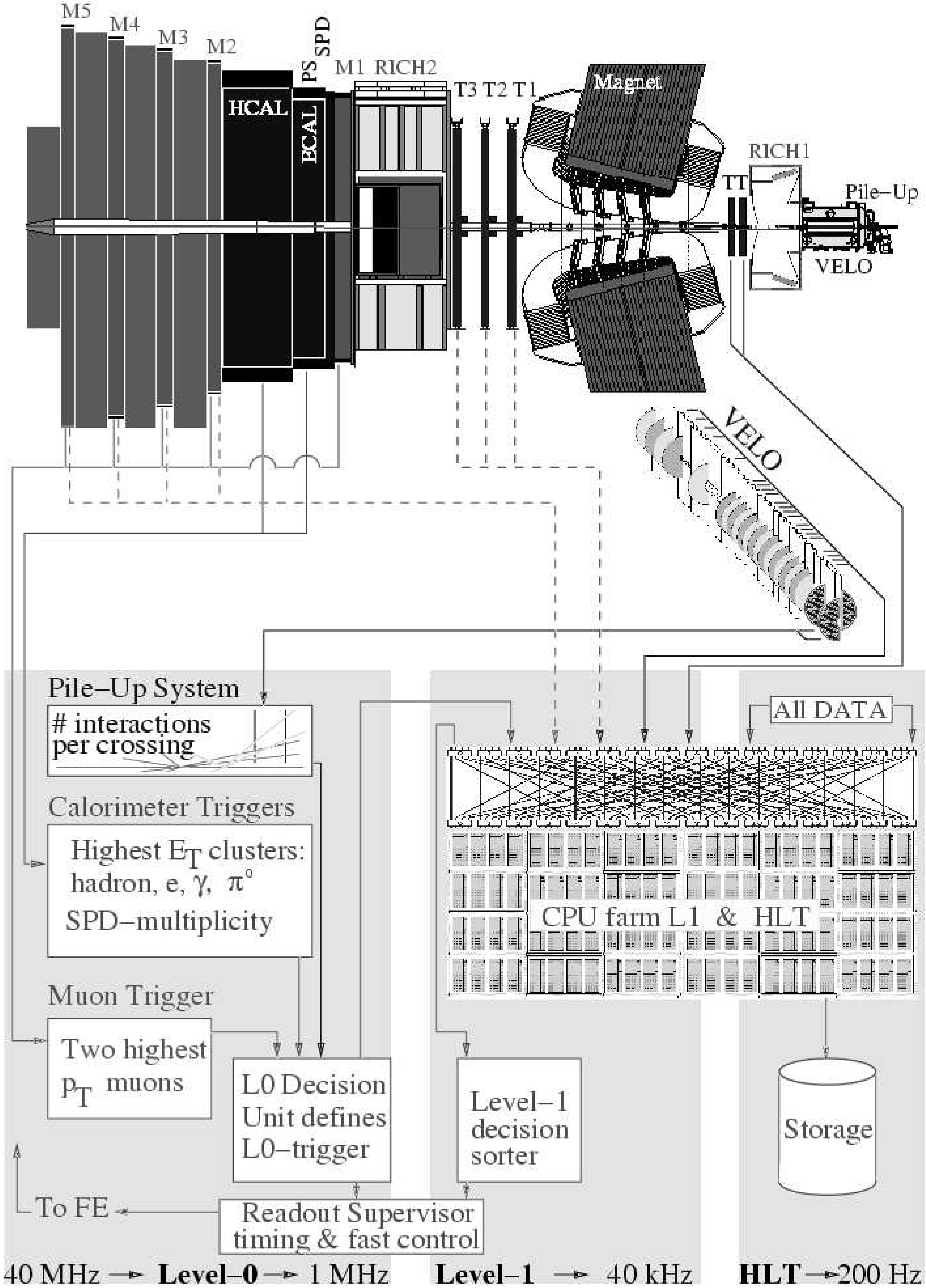

Figure 18: *The LHCb detector and the trigger system. The collision point, situated next to the Vertex Locator (VELO) defines the origin. The coordinate system is right-handed and has the origin in the collision point, at the Vertex Locator (VELO). The z-axis is pointing in the direction of the muon chambers and the y-axis is pointing upwards in the picture. The magnetic deflection of a charged particle with an initial trajectory parallel to the z-axis will be in the x-direction. [24]*

3.2 The LHCb trigger

The LHCb trigger is based on three trigger levels, level 0 (L0), level 1 (L1) and the High Level Trigger (HLT). The L0 trigger will reconstruct the electron, photon and hadron cluster with the highest p_{T} in the calorimeter and the two highest p_{T} muons from the muon chambers. If certain E_{T}-cuts are satisfied the event will be passed to L1. The output from L0 is limited to 1 MHz. All operations and calculations at L0 are performed on front-end(FE) electronics boards. Each board can handle 32 calorimeter cells and by adding the E_{T} of regions of 2×2 cells the highest E_{T}-cluster per board is chosen. For the electromagnetic calorimeter, this results in a maximum of 28 clusters, one for each FE-board. By using information from the SPD and the PS the electromagnetic clusters can be classified as electron-candidates or photon-candidates. A cluster that is classified as an electron is called a L0-electron. So, when talking about L0-electrons one is not referring to electrons but rather to clusters of electron-type. Clusters in the hadronic calorimeter become hadron-candidates. The results from L0 are stored in the L0 Decision Unit(L0DU). The Level 1 trigger reduces the L0 1 MHz signal from to 40 kHz. It is implemented on a farm of commodity computers. For the trigger decision the L0DU summary, VELO tracks and TT tracks are available. By matching VELO tracks to the clusters a momentum measurement is obtained. The HLT further reduces the trigger rate to 200 Hz. It will operate at the same computer farm as L1 and have access to the full event thus refining the L1 decision.

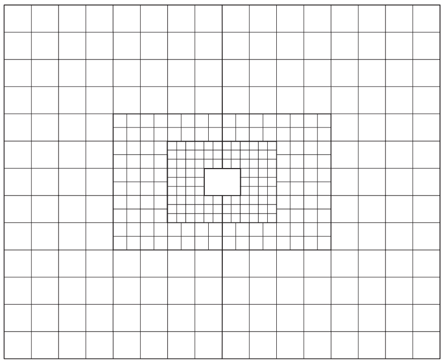

Figure 19: *The ECAL as it is seen from the interaction point. The beam pipe is located at the centre of this figure. As can be seen, the cell size is not the same everywhere. Closest to the beam pipe the cells have the length 40.4 mm, the middle cells have 60.6 and the outermost have 121.2 mm. A particle affected by the magnetic field will be deflected along the x-axis which runs horizontally in the figure.*

3.3 The efficiency to find electrons from $\mathrm{B_d^0} \to \mathrm{J}/\psi(e^+e^-)$

Since the study is done from a L1 point of view the calorimeter information available is the clusters that were formed in L0 and separated into L0-electrons and L0-photons. Apart from the position and energy measurements, the trigger simulation

also supplies truth information about the particle that caused the cluster.
In the dielectron trigger it is necessary to find at least two L0-electrons. Electrons from a B-decay are expected to have a higher E_{T} than background particles so it is the L0-electrons with the highest E_{T} that will be interesting to this study. In what follows, the highest E_{T} L0-electron will be referred to as the 1^{st} and the next L0-electron in E_{T}-order will be called the 2^{nd} . Furthermore, the term J/ψ-electron will refer to a L0-electron with a mother or grandmother being a J/ψ from a $\mathrm{B_d^0}$. Grandmother particles are included since there is a possibility for the electron to radiate a bremsstrahlung photon just before hitting the ECAL. The electron and the photon will then cause a cluster at the same position in the ECAL. If the photon carries a large fraction of the electron's energy the truth particle the trigger simulation associates the ECAL cluster with the photon and the J/ψ becomes the grandmother of that cluster. The L0 trigger will still consider the deposited energy in the ECAL to come from an electron (due to the electron identification capability of the SPD) and therefore the cluster will be classified as a L0-electron.
The efficiency of using calorimeter clusters depends on the efficiency to find the two electrons from J/ψ among the highest E_{T} L0-electrons. Table 3 shows statistics concerning this matter. Two subsets of a signal sample were used to produce the table. Events that passed L0 are in the 'after L0' columns and events that passed both L0 and would pass a later offline selection are in the 'after L0 and offl. sel.' columns. In ~19 % of the L0+offline selected events the 1^{st} and 2^{nd} electrons originate from a J/ψ-decay. If also the 3^{rd} is taken into account this figure increases to a value close to 30 %. Although only 1^{st} and 2^{nd} are included in this study one can keep in mind that the inclusion of the 3^{rd} candidate has the potential to increase the trigger efficiency.

Event Sample:	after L0	after L0 and off.sel.
1^{st} and 2^{nd}	$7.7 \pm 0.1\%$	$18.8 \pm 1.1\%$
1^{st} and 3^{rd}	$3.1 \pm 0.1\%$	$7.1 \pm 0.7\%$
2^{nd} and 3^{rd}	$1.5 \pm 0.1\%$	$3.3 \pm 0.5\%$

Table 3: *The fraction of events in each sample when both J/ψ-electrons are among the three highest E_{T} electrons. L0 sample contains ~50000 events and L0+offline selection sample contains ~1200 events.*

3.4 Understanding the L0-electrons

3.4.1 Clones

The electromagnetic calorimeter(ECAL) is placed in the xy-plane of the detector. The cell size is not constant but grows with the distance to the beam pipe. Fig. 19 shows the ECAL and its differing cell sizes. As explained in Sec. 3.2 28 FE-boards are used to read off the calorimeter cells, and the highest E_{T} EM cluster is chosen in each board, resulting in a maximum of 28 EM clusters. If a particle hits the ECAL in the border between two FE-boards its energy will be deposited both boards. If the energy is high enough, there is a chance that this appears as two different,

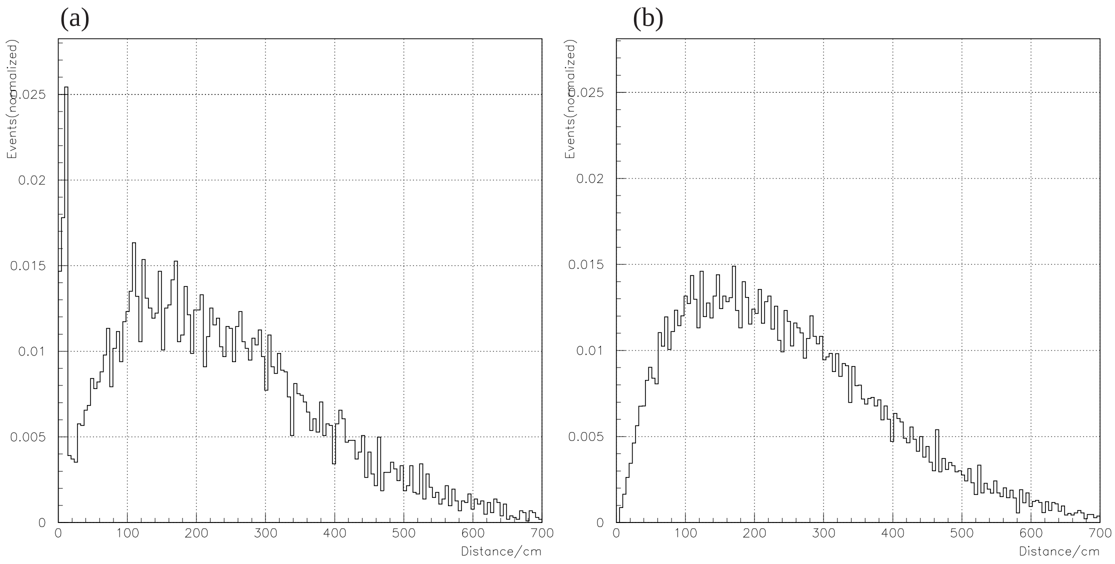

Figure 20: *Distance between* 1^{st} *and* 2^{nd} *a) without and b) with a distance cut applied. The peak near 0 in (a) is to great extent due to clones.*

neighbouring particles. The ECAL is constructed so that the FE-boards can access cells in adjacent boards when summing the E_{T} of regions of 2×2 cells. The result is that two FE-boards can have access to the same cells delivering one cluster each, and these two clusters will be at almost the same position and with almost the same energy. Only one of the clusters is relevant, the other can be regarded a clone of the first one.
To detect a clone a distance cut is used. Fig. 20a shows a distance plot between the 1^{st} and 2^{nd} L0-electron. The big peak at 0 is clearly due to clones. In Fig. 20b the distance cut has been applied. If two L0-electrons are found in adjacent ECAL cells the one with the lower $E_{\mathrm{T}}$is considered to be the clone. To decide if two L0-electrons are in adjacent cells the minimum distance between clusters is set to be 1.5 times the cell size. If the two L0-electrons are located in areas with different cell size (See Fig. 19, the biggest cell-size is chosen.

3.4.2 Energy resolution

The offline resolution of the ECAL varies with the amount of deposited energy in a cluster. In the calorimeter TDR [25] it is quoted to be

$$\frac{\sigma_E}{E} = \frac{9.5\%}{\sqrt{E}} \oplus 1\% \quad (E \,\mathrm{in\, GeV}) \; .$$

At L1 the resolution is completely dictated by the dynamic range of the trigger readout of the calorimeter. The analogue energy measurement in the calorimeter is not used at trigger level but an E_{T} value is calculated instead. Doing this involves converting a digitized 12-bit E to a 8-bit E_{T} with the consequence that the E_{T} measurement becomes saturated. The saturation has been set to 5.1 GeV [24]. Due to this, the offline energy resolution is not valid at L1. To estimate an empiric

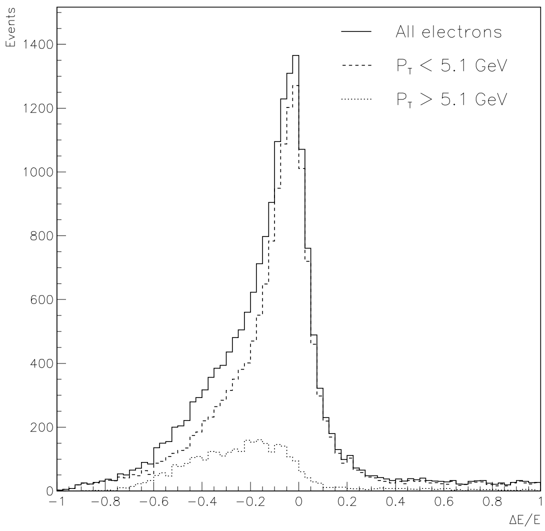

Figure 21: *Energy resolution for J/ψ-electrons. The effect of the 5.1 GeV E_{T}- saturation can be seen. The electrons with a true E_{T} over 5.1 GeV constitute a non-negligible part of the low-energy tail.*

approximation for the resolution of J/ψ-electrons the quantity

$$\frac{\Delta E}{E} = \frac{E_{cal} - E_{true}}{E_{true}}$$

was used. E_{true} is the generated energy of the particle that caused the cluster and E_{cal} is the energy measured in the calorimeter. This calorimeter energy is calculated from the E_{T} which introduces the E_{T}-saturation in the resolution approximation. Fig. 21 shows the impact of the saturation on a $\Delta E/E$-plot. The left tail can be explained by bremsstrahlung losses but also by the saturation. If the peak is decomposed into two distributions, one for electrons with true $E_{\mathrm{T}} > 5.1$ GeV and one for electrons with true $E_{\mathrm{T}} < 5.1$ GeV the effect can be seen.

When the quantity $\Delta E/E$ is plotted for the J/ψ-electrons a peak around 0 appears. The RMS of the peak gives the mean resolution for all the energies included in the plot. To investigate if an energy dependence exists, the RMS value of $\Delta E/E$ is plotted versus the generated energies of the J/ψ-electrons. The result is shown in Fig. 22. To a first approximation the resolution can be taken to be constant at different energies with a mean value of about $\Delta E/E \approx 10\%$.

3.5 Bremsstrahlung reconstruction

There is a probability for the electrons to interact with nuclei in the detector and thereby emit bremsstrahlung radiation. If this is done after the magnet the photons will be deposited in the same cells as the electron and no energy will be lost. While passing the magnet, the probability of bremsstrahlung radiation is small since that part is free from detector material. The photons emitted before the magnet will continue their initial trajectory while, due to their charge, the electrons are deflected by the magnetic field. By measuring the energy of the L0-electron it can be calculated

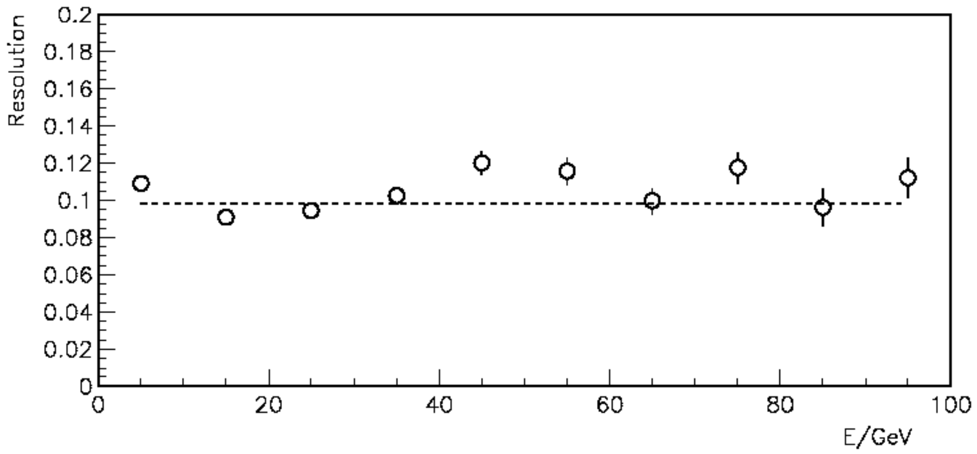

Figure 22: *The energy resolution of* J/ψ*-electrons versus their generated energy.*

how big its magnetic deflection was but one can not determine in which direction the particle was deflected since the sign of the charge of the particle causing the L0-electron is unknown. But, since the deflection is along the x-axis, by adding and subtracting the calculated deflection to the x-position of the L0-electron, two points can be predicted where the bremsstrahlung photons should be found. A successful bremsstrahlung recovery can increase the energy resolution of the electron clusters resulting in higher trigger efficiencies.

3.5.1 Finding bremsstrahlung

The uncertainty involved in the prediction of where the bremsstrahlung photons should be found excludes the use of an isolated predicted point. Instead an area, a window, around the point has to be defined. The dimensions of this window should depend on the uncertainty of the predicted point. This uncertainty depends on the error in the position measurement and the error of the calculated deflection due to the magnetic field. The error in x is given by

$$\sigma_x = \sqrt{(\sigma_{xpos})^2 + (\sigma_{deflection})^2}.$$

As σ_{xpos} we use the size of the ECAL cell where the electron was found (a deliberate overestimate compared to the conventional use of σ=[**cell size**]/$\sqrt{12}$). Since $\sigma_{deflection}$ is a function of the energy, it can be approximated with

$$\sigma_{deflection} \approx \sqrt{\left(\frac{\mathrm{d}f(E)}{\mathrm{d}E}\bigg|_{E=E_e}\right)^2 \cdot \sigma_E^2}$$

where $f(E)$ is the function that describes how the deflection depends on the energy and σ_E is estimated to be $E \cdot 10\%$, based on Fig. 22. The behaviour of σ_x can be seen in Fig. 23. σ_y is taken to be the size of the cell where the electron was found.

As in the case of σ_x this is an overestimate. In Fig. 24 the purity of the detected bremsstrahlung candidates is shown. The purity is defined to be the fraction of the bremsstrahlung candidates that are photons from a L0-electron. As seen in Fig. 24a, the purity drops outside the 1 σ_x region, from a maximum value of 80 % real bremsstrahlung photons near the predicted x-value. Fig. 24b in a similar way shows that a y-size of 1 σ_y should be enough to detect the real bremsstrahlung. To be on the safe side a window of $\pm 1.1\ \sigma_x$ and $\pm 1.1\ \sigma_y$ is used. The full set of L0-electrons and L0-photons are examined to find the bremsstrahlung. If many candidates are found within the same window, the one closest to the predicted point is picked. L0-electrons are included to maximise the recovery potential.

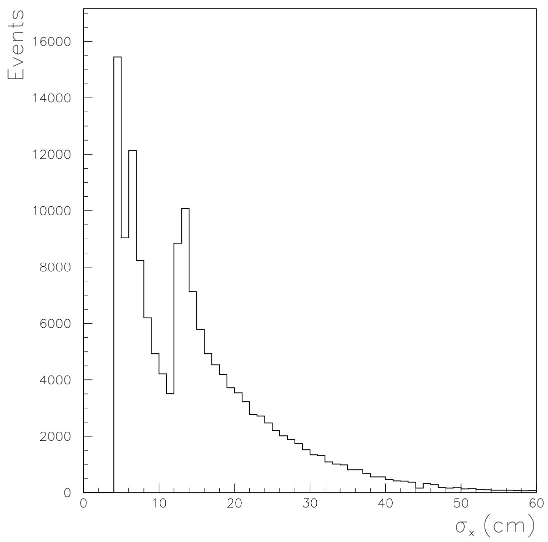

Figure 23: *The uncertainty σ_x, used to calculate the bremsstrahlung window can assume values in a broad range. The three peaks are due to the three different cell sizes in the calorimeter.*

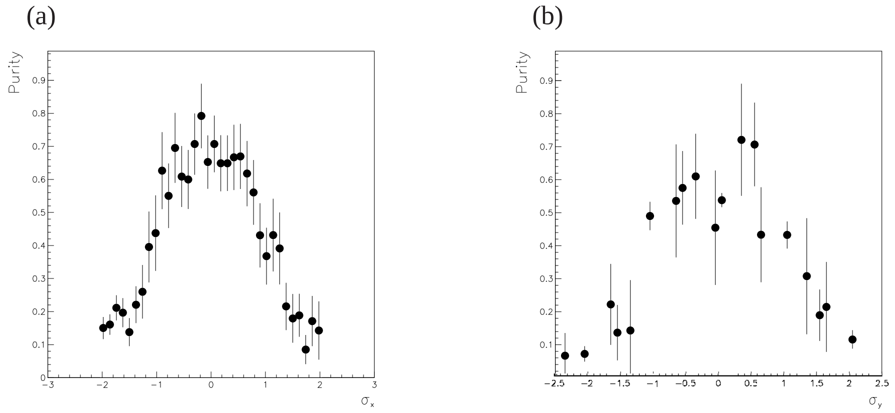

Figure 24: *Purity of bremsstrahlung candidates detected at distance a) σ_x, and b) σ_y from the predicted point. The plots are in units of σ_x and σ_y.*

The outcome of the bremsstrahlung search can be found in Table 4. In the table, Pos.Win. means 'positive window' and it refers to the window around a predicted point where the bremsstrahlung of a positively charged particle would be found. Neg.Win. is defined in a analogous manner.
The table shows the the amount of J/ψ-electrons and positrons without a bremsstrahlung candidate, with a candidate and with a true candidate (i.e. a real bremsstrahlung photon) in the positive and negative window. As expected, more bremsstrahlung candidates are found in the pos.win. than in the neg.win. for an

e^+ and vice versa.
For the offline selected events a bremsstrahlung candidate is found only in ∼10% of the cases but the purity is very high, ∼ 90%. A bremsstrahlung reconstruction can be made by adding the energy of the bremsstrahlung candidate to the energy of the L0-electron.

J/ψ-electrons	after L0			after L0 and offl.sel.		
	w/o cand.	w. cand.	true cand.	w/o cand.	w. cand.	true cand.
e^+ Pos. Win.	6412	1393	1231	249	63	55
e^+ Neg. Win.	7693	123	9	312	5	0
e^- Pos. Win.	7713	142	15	292	3	0
e^- Neg. Win.	6397	1458	1256	295	53	51

Table 4: *Statistics for bremsstrahlung candidates connected to* J/ψ*-tagged electrons. The table contains the results for events that have passed L0 and events that would both pass L0 and be selected by offline software. A sample of 19052 (708)* J/ψ*-electrons from L0 events (L0+offline selected events) was used.*

3.6 The charge of the L0-electrons

To go a step further with the L0-electrons they can be used in an invariant mass plot to select good J/ψ-events. In the ATLAS analysis, tracks were used for the invariant mass cut. This will not be the case here. Instead the possibility to use only calorimeter information is evaluated.
The first challenge when not using tracks is to determine the charge of a particle that causes a L0-electron. The electron and the positron from the J/ψ decay have opposite charges and therefore their trajectories will be bent in opposite directions when they are traversing the magnetic field. The magnetic field in the trigger simulation is oriented in such a way that the positrons will turn in the positive direction of the x-axis. For electrons it is the opposite. From this an assumption about the charge of the L0-electrons is made: When looking at two L0-electrons, the one with the highest x-value is considered to be the positron and the other is considered to be the electron. Table 5 shows how the J/ψ-electrons are distributed. Although the assumption is not totally right it is certainly good.

J/ψ-electrons	after L0	after L0 and off.sel.
$x_{e^+} > x_{e^-}$	83.6 ± 0.8 %	84.3 ± 2.8 %
$x_{e^+} < x_{e^-}$	16.4 ± 0.8 %	15.7 ± 2.8 %

Table 5: *Fraction of* J/ψ*-positrons(electrons) that have a greater(smaller) x value than the electron(positron) from the same decay.*

To enhance the charge tagging the results from the bremsstrahlung search can be used. If a possible bremsstrahlung photon is found in the window corresponding to a positron, we may use this to tag the L0-electron as being positively charged. In the cases where none of the electrons have a bremsstrahlung candidate, when one electron has a candidate in each window or when both electrons have a candidate in the positive/negative window (indicating the same charge), the ambiguity is resolved by applying the other method described above.

3.7 The invariant mass

The E_T, position and assumed charge of the 1^{st} and 2^{nd} L0-electrons can now be used to produce an invariant mass plot. A E_T-cut will also be used to suppress the background. As in the case of ATLAS, the minimum bias events (the background) will dominate the trigger rate. The background efficiency should be in the order of $\epsilon_{bg} \approx 0.1\%$. Three E_T-cuts have been investigated:

- A loose cut: $E_\mathrm{T}(1)>1.5$ GeV , $E_\mathrm{T}(2)>0.85$ GeV .
- A medium cut: $E_\mathrm{T}(1)>3.0$ GeV , $E_\mathrm{T}(2)>1.5$ GeV .
- A tight cut: $E_\mathrm{T}(1)>3.0$ GeV , $E_\mathrm{T}(2)>1.5$ GeV

Also, the reconstructed bremsstrahlung energy has been added to the L0-electrons. In Fig. 25a the invariant mass of L0-electrons from a sample of signal events that have passed L0 can be seen, before and after a bremsstrahlung reconstruction. The tight E_T-cut was also used. The reconstruction is not significantly changing the distribution, but a shift to higher masses can be seen for events in region below the nominal J/ψ-mass of 3.1 GeV.
Fig. 25b shows the invariant mass for a the loose cut on a sample of L0+offline selected events. Superimposed is the minimum bias sample. The signal is normalised to the total number of L0+offline selected events while the minimum bias sample is normalised to the amount of background events that pass L0. The peak obtained is not very sharp. A big tail towards lower masses can be seen. Although a bremsstrahlung reconstruction has been performed, the tail shows that a lot of bremsstrahlung could not be found by the algorithm. The 5.1 GeV saturation discussed in Sec. 3.4.2 also gives a shift towards lower masses. Fig. 25c and d show the same as 25b but for the medium and tight E_T-cuts.
As marked in Fig. 25d, a mass cut at 2.1 GeV $\leq$ m $\leq$ 3.3 GeV covers the J/ψ-mass peak well. This mass cut is not symmetric around the correct J/ψ-mass in order to not reject too many of the events where the L0-electrons have a lower measured energy than they initially had after the J/ψ-decay. To suppress the background efficiency enough the tight cut is required in this case, resulting in an efficiency of 18% and a background efficiency of 0.38%.

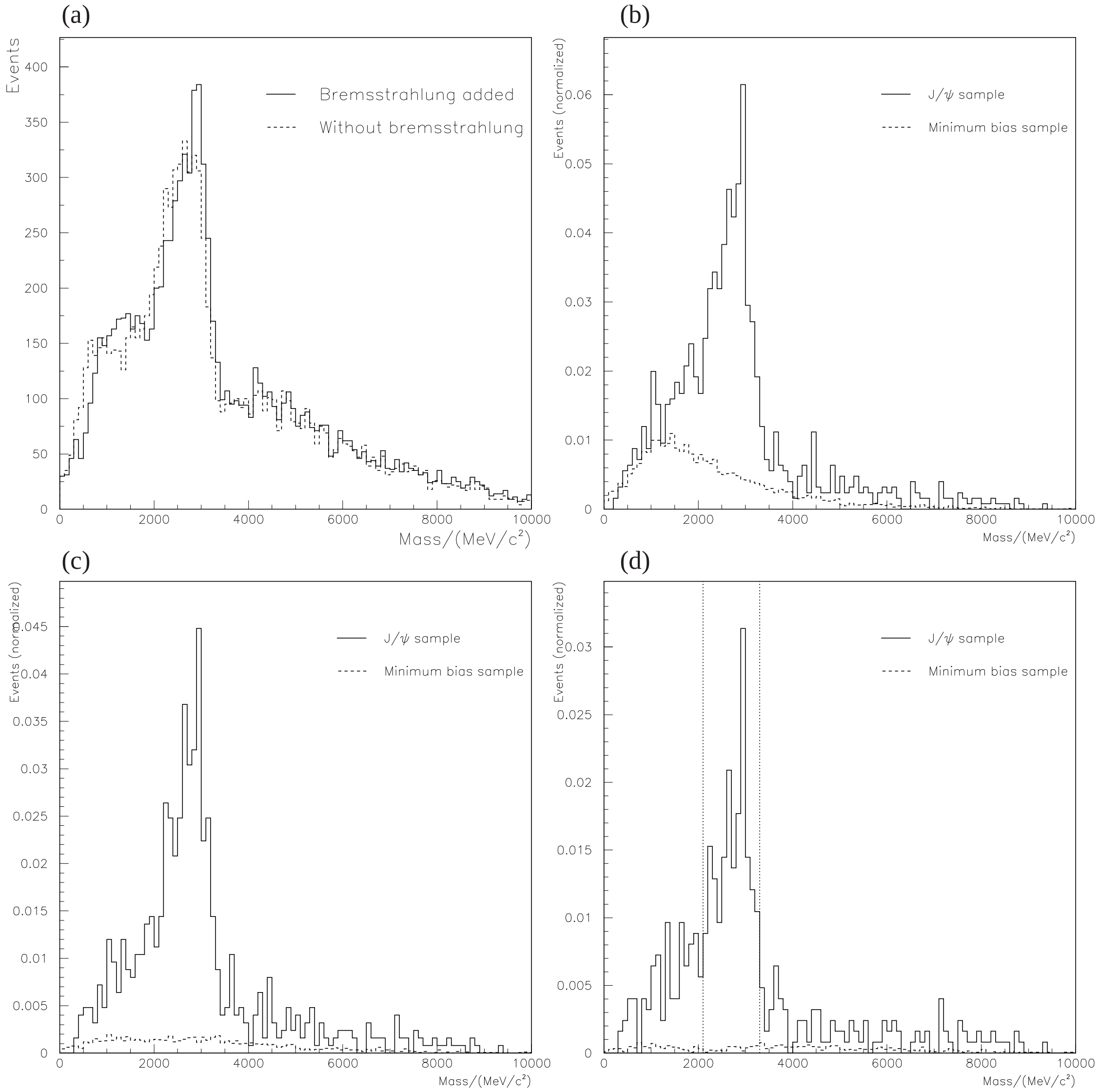

Figure 25:
a) The effect of a bremsstrahlung reconstruction on the mass plot of L0-electrons from a sample of L0 selected signal events. The tight E_{T}-cut has been used.
b)-d):
The invariant mass of L0-electrons from an L0+offline selected sample and a minimum bias sample, with different E_{T}-cuts.
b) Loose cut at $E_{\mathrm{T}}(1)>1.5$ GeV , $E_{\mathrm{T}}(2)>0.85$ GeV .
c) Medium cut at $E_{\mathrm{T}}(1)>2.8$ GeV , $E_{\mathrm{T}}(2)>1.0$ GeV .
d) Tight cut at $E_{\mathrm{T}}(1)>3.0$ GeV , $E_{\mathrm{T}}(2)>1.5$ GeV .

3.8 Conclusion

Using an algorithm to locate bremsstrahlung photons in the ECAL the resolution of the $J/\psi(e^+e^-)$ invariant mass can be improved, and the bremsstrahlung photons can be used to determine the charge of the electron. A tight E_T-cut of $E_\mathrm{T}(1)>3.0$ GeV , $E_\mathrm{T}(2)> 1.5$ GeV is needed to suppress the background to reasonable levels. If a background retention as high as 0.38% can be accommodated within L1, the method of this study gives an efficiency of 18% for an L0+offline selected sample. Other channels containing a $B \rightarrow J/\psi(e^+e^-)$ decay would also benefit from this. To investigate the full potential of a dielectron trigger tracks have to be included.

It was also studied, although not exploited in this note, that using the three highest E_T candidates (instead of just the two highest) raises the probability to find both electrons from J/ψ. It was found that in $\sim 29\%$ of the offline selected events two out of the three highest $E_\mathrm{T}$electrons originate from a J/ψ.

4 Comparing the two studies

In this thesis two trigger studies have been presented, one ATLAS and one LHCb study. The two experiments differ a lot in their choice of detector. LHCb, being a experiment dedicated to the study of B-hadrons is designed as a one-arm spectrometer while the general purpose detector ATLAS covers a large fraction of the 4π-space. Being a dedicated detector LHCb is optimized for its task. By running at a luminosity 10-50 times lower than ATLAS multiple interactions per bunch crossing are suppressed leading to a cleaner trigger environment in terms of cluster and track multiplicities. ATLAS instead, with a bigger angular coverage and running at a higher luminosity, can afford to lose events and still be competitive with its B-physics programme.

The $\mathrm{B_d^0} \to \mathrm{J}/\psi(e^+e^-)\mathrm{K_s}$ decay is of interest to both experiments since it provides a clean way to measure $\sin 2\beta$ in the unitarity triangle. In ATLAS, a RoI-guided trigger for $\mathrm{B_d^0} \to \mathrm{J}/\psi(e^+e^-)\mathrm{K_s}$ was evaluated. The RoI-guidance means that the trigger relies heavily on the electromagnetic calorimeter which also is the case on LHCb . Since every experiment has its own language the RoI-guidance at LHCb is called a dielectron trigger. The essence of the two triggers is the same, to find the EM clusters from the electrons and use them in the second trigger lever, on ATLAS called level 2(LVL2) and on LHCb called level 1(L1). In ATLAS the clusters were used to guide the track reconstruction to limit the resource requirements. It was found that compared to the full-scan trigger, the signal efficiency was deteriorated to about 10% for all LVL1 accepted events but the background retention was about 0.3% which makes the trigger feasible. In the LHCb study, no tracks were used, it was purely based on calorimeter clusters. To increase the efficiency a bremsstrahlung reconstruction was attempted. On ATLAS this is done with sophisticated methods not earlier in the last level of the trigger, the Event Filter. The LHCb study examined a very simple method, a resource efficient strategy to find bremsstrahlung. However, the results of the bremsstrahlung reconstruction were modest. A signal efficiency of 18% was obtained for offline accepted events, giving a background retention of 0.38%.

To work with the same topic on two large experiments gives a good opportunity to compare methods, ideas, and choices of design. The trigger simulation on LHCb seems to be more developed and complete than the ATLAS trigger simulation. For this reason, it is not straightforward to compare the efficiency figures that have been obtained in the two studies. For instance, at ATLAS a full simulation of the level 2 trigger was not available and offline algorithms had to be used as a complement. In the LHCb study on the other hand, a sample of offline selected events were used to calculate the trigger efficiency. Common though for both the studies is that they investigate new possibilities of the trigger and that the results from this thesis most probably will be followed up by others.

Acknowledgments

Thanks a lot to Paula Eerola, Niels Tuning and John Baines for answering my numerous questions about ATLAS, LHCb and the trigger simulations and helping me to progress in my work. Without you this would not have been possible. Also thanks to Chafik Driouichi and Robert Siljan for valuable discussions and good company. Thanks to the guys at Vinterpalatset for the *fika* breaks and to Malin Sundqvist for standing by my side.

References

[1] S.H. Wu et al., Phys. Rev. 105, 1413-1415 (1957).

[2] M. Goldhaber et al., Phys. Rev. 109, 1015-1017 (1958).

[3] J. C. Palathingal, Phys. Rev. Lett. 24, 524-526 (1970).

[4] J. H. Christenson, Phys. Rev. Lett. 13, 138-140 (1964).

[5] W.T. Ford, *Measurements of* $\sin 2\beta$ *in B-decays*, hep-ex/0309001.

[6] The ATLAS Collaboration, *ATLAS detector and physics performance Technical Design Report, Volume II*, CERN/LHCC 99-15.

[7] The LHCb Collaboration, *LHCb Technical Proposal*, CERN/LHCC 98-4.

[8] The ATLAS collaboration, *ATLAS Trigger Performance Status Report*, CERN/LHCC 98-15

[9] The ATLAS Collaboration, *ATLAS Technical Proposal*, CERN/LHCC 94-43.

[10] The ATLAS Collaboration,*ATLAS First-Level Trigger Technical Design Report*, CERN/LHCC 98-14.

[11] The ATLAS Collaboration, *ATLAS detector and physics performance Technical Design Report, Volume I*, CERN/LHCC 99-14.

[12] *The Athena Web Site*, atlas.web.cern.ch/Atlas/GROUPS/SOFTWARE/OO/architecture/General

[13] A. Watson, E. Moyse, *Performance and Validation of TrigT1Calo, the Offline Level-1 Calorimeter Trigger Simulation*, ATL-COM-DAQ-2003-027.

[14] The PESA CORE ALGORITHMS GROUP, *Algorithms of the ATLAS High Level Trigger*, ATL-DAQ-2003-002.

[15] J. Baines et al. , *Performance studies of the High Level Electron Trigger*, ATL-COM-DAQ-2003-020.

[16] J. Baines et al. , *B-Physics Event Selection for the ATLAS High Level Trigger*, ATLAS-DAQ-2000-031.

[17] The ATLAS Collaboration,*ATLAS High-Level Triggers, DAQ, and DCS Technical Proposal*, CERN/LHCC 2000-17.

[18] B. Epp, V.M. Ghete, A. Watson, *A study of the use of Low* E_T *calorimeter RoI in the ATLAS B-Trigger*, ATL-COM-DAQ-2003-036.

[19] The ATLAS Collaboration, *ATLAS High-Level Trigger, Data Acquisition and Controls Technical Design Report*, CERN/LHCC 2003-022.

[20] J. Baines et al., *Resource Estimates for the ATLAS B-Physics Trigger*, ATL-COM-DAQ-2002-013.

[21] P. Eerola, *The inclusive muon cross-section in ATLAS*, ATL-MUON-98-222.

[22] P. Ball et al. , *B Decays at the LHC*, CERN-TH/2000-101, hep-ph/0003238.

[23] A. Papadelis, *Study of the use of dielectrons from* $B \to \mathrm{J}/\psi(e^+e^-)$ *at L1*, LHCb 2003-096 TRIG

[24] The LHCb Collaboration, *LHCb Trigger System Technical Design Report*, CERN/LHCC 2003-031.

[25] The LHCb Collaboration, *LHCb Calorimeter Technical Design Report*, CERN/LHCC 2000-0036.